Investigating the Effect of the Fluid Properties on Bubble Dynamics and Heat Transfer in a Tapered Microgap with Multiphase Flow Modeling

Divyprakash Pala, Maharshi Y. Shuklab, Satish G. Kandlikarc, Isaac Perez-Rayad,*

- ^a Mechanical and Industrial engineering department, Rochester Institute of Technology, Rochester, New York-14623, United States of America
- ^b Mechanical and Industrial engineering department, Rochester Institute of Technology, Rochester, New York-14623, United States of America
- ^c Mechanical and Industrial engineering department, Rochester Institute of Technology, Rochester, New York-14623, United States of America
- ^d Mechanical and Industrial engineering department, Rochester Institute of Technology, Rochester, New York-14623, United States of America
- *Corresponding author

E-mail addresses: a dp8120@rit.edu, b ms1235@rit.edu, sgkeme@rit.edu, d,* ibpeme@rit.edu

Abstract

Nucleation and bubble dynamics on a heater surface contribute to high heat transfer rate in pool boiling. Introducing two-phase flow in narrow channels further improves heat transfer. Use of expanding taper microgap geometry further enhances heat transfer, and proper balancing of taper angles and flow lengths leads to self-sustained flow boiling in tapered microgap geometries. This paper focuses on understanding the underlying enhancement mechanism by studying the bubble behavior as they expand and accelerate in the direction of increased taper. The present study conducts a 2D simulation analysis of bubble growth in tapered microgaps with numerical simulations to identify the effect of the fluid properties and tapered angle in the bubble and fluid dynamics behavior. Ansys-Fluent is customized with user-defined-functions (UDFs) accounting for the interfacial heat and mass transport, including a sharp interface and direct calculation of mass transfer with temperature gradients. The study was conducted using air injection and boiling simulation from the conception to the departure of a bubble. The tapered angles were 5°, 10°, and 15°, with flowrates between 3 ml/min to 30 ml/min, 1 mm air inlet, and at 1 mm distance from the convergent end. The departure time of 10 subsequent bubbles was recorded to check the configuration with the quickest bubble removal. A critical flowrate and surface tension region was established for the escape direction of the bubble. In addition, the numerical simulation considered the tapered microgap with a nucleating bubble at atmospheric conditions with a wall superheats of 5 K. The results show that the bubble growing over the heated surface creates fluid circulations and interfacial conditions that suppress the thermal boundary layer leading to an increased local heat transfer coefficient within a range of 1 mm from the interface.

Keywords:

2D, VOF, sharp interface, tapered microgap, boiling, Ansys Fluent.

Nomenclature:

 \vec{g} gravity m/s^2

```
\rho density (kg/m<sup>3</sup>)
```

t time (s)

 \vec{u} velocity vector (m/s)

 μ liquid viscosity (Pa · s)

 F_q fluid volume fraction (dimensionless)

κ curvature of the interface

 ∇ gradient operator

 F_s/σ surface tension (N/m)

h_{fg} latent heat of evaporation (KJ/kg)

 α thermal diffusivity (m²/s)

C convergent end of the taper block

D divergent end of the taper block

 Q_l flowrate (ml/min)

h heat transfer coefficient (W/m²K)

 k_l thermal conductivity (W/mK)

T Temperature (K)

t time (s)

Subscripts

g gas phase

l liquid phase

w wall

s saturation

1. Introduction

In many industrial heat exchange systems, boiling plays a crucial role due to its ability to dissipate high heat transfer at relatively small surface temperatures. Pool boiling has emerged as an excellent solution in phase-change-based thermal management systems. With various surface modifications, pool boiling has been instrumental in assisting supercomputer processors and data centers to achieve high heat dissipation under normal operating conditions [1]–[4]. Similarly, pool boiling is instrumental in passive decay heat removal from tubes in nuclear power plants, heat exchangers, and evaporators [5]–[7]. Other applications include high heat transfer in air conditioning and refrigeration systems [8] and electric vehicle batteries [9], [10]. Although boiling dissipates high heat fluxes at low wall superheats, the chaotic conditions caused by rapid growth, coalescence, and liquid rewetting can result in increased pressures,

reduced flowrates, additional instabilities, or even flow reversal in the system [11]–[13]. This also leads to difficulties in flow visualization and analyzing the thermal and fluid dynamic conditions. Computer simulations are a powerful tool that has helped study the microlayer [14]–[16] ,bubble shape [17], [18] , isotherms [19], and bubble behavior [20], [21] to have a better understanding of the thermal and fluid behavior associated with boiling.

Heat transfer enhancement in pool boiling can be achieved using active and passive methods [22]. Active methods include the usage of a pump as a source for circulation of coolants such as jet impingement [23]— [25], spray cooling [26]–[28], and external power input such as mechanical vibration [29], and magnetic field [30]. The typical passive techniques include enhanced surfaces [5], [8], [31]–[34], nanofluid [35], and artificial nucleation sites [36]. The advantages of passive systems include (i) less energy consumption, (ii) less noise, and (iii) more reliability due to fewer moving parts. Recent advances include the development of a specific type of passive system using tapered geometry. Kandlikar [37] studied the flow instabilities due to nucleation in microchannels using high-speed visual observations. Mukherjee and Kandlikar [38] numerically studied bubble growth in a microchannel and proposed using tapered microchannels to reduce flow instabilities. Kandlikar et al. [39] used open microchannels with a tapered microgap to significantly reduce pressure drop compared to a uniform cross-section gap. Balasubramanian et al. [40] dissipated more than 400 W/cm² heat flux using stepped microchannels and reduced pressure drop by 30% by expanding microchannels. Kalani and Kandlikar [41] examined bubble flow patterns in plain and microchannel setups under tapered microgaps, finding that rapid bubble growth did not affect flow stability. Introducing open microchannels with the tapered manifold in flow boiling achieved high heat fluxes at minimal pressure drops. A 6° taper enhanced bubble expansion, promoting pressure recovery and improving heat transfer. Consequently, they achieved a critical heat flux (CHF) of 1.07 kW/cm² with a mere 30 kPa pressure drop. Pressure recovery in a tapered system was further evaluated and showed an effective decrease in pressure drop in flow boiling. Moreira et al. [42] proposed a converging and diverging manifold and indicated that the pressure drop of converging and diverging gaps was higher than that of uniform gaps but with a significant heat transfer improvement. Emery et al. [43] developed a thermosiphon-based CPU cooler using the tapered microgap and HFE 7000 as the working fluid to dissipate a heat flux of over 44 W/cm². Chauhan and Kandlikar [44] further improved the thermosiphon loop performance by testing symmetrical dual taper and dissipating more than 280 W of heat without reaching CHF. Chauhan and Kandlikar [37] proposed using single tapered and symmetrically tapered microgaps in water [45] and HFE 7000 [46] to transform pool boiling into a self-sustained flow boiling mechanism. In prior research by our group, we examined tapered microgaps with various angles (5°, 10°, 15°, 20°, and 25°) and inlet gaps of 0.8 mm and 1.27 mm, utilizing HFE 7000 as the working fluid. A 25° taper angle yielded a 2x HTC enhancement with a 0.8 mm inlet gap and 1.5x with 1.27 mm. We also tested water-filled tapered microgaps with 10° and 15° angles 1.27 mm inlet gap, observing over 2x improvements in critical heat flux (CHF) and HTC compared to plain chips [47]. Although significant progress has been made, there still exists scope for performing parametric study using different fluids, varying surface tension of the fluid, and using air-injection study to focus on the behavior of individual bubbles in a tapered microgap.

Numerical simulations for boiling have been carried out for flow and pool boiling in microchannels using tools like OpenFOAM [48], [49], Lattice-Boltzmann method [50]–[53], in-house codes [15], and Ansys Fluent [54], [55]. Multiple studies were carried out for flow within a microchannel based on shape, flow pattern, artificial cavities, manifold arrangement, surface roughness, and wettability [48], [56]–[63].

Mukherjee and Kandlikar [57] simulated the growth of a spherical bubble during flow boiling in a square microchannel using the level set method. They observed that the presence of the channel walls tended to elongate the bubble. Magnini and Matar [48] studied the effect on liquid film distribution and heat transfer using square and rectangle microchannels. They found out that for lower flowrates, square microchannels, and for higher flowrates, rectangular microchannels yielded better results. Mukherjee and Kandlikar [38] analyzed the effect of inlet constrictions to prevent the backflow growth of vapor bubbles in a square microchannel. Although they positively stabilized the flow, it generated a high-pressure drop and reduced the efficiency. Diverging microchannels toward the desired flow were proposed as a better solution. Alugoju et al. [64] conducted a comparative numerical study for a flow boiling system using a straight and a diverging microchannel. They varied the diverging angle between 0° to 8° and used a constant heat and mass flux. The results showed that increasing the channel angle alters bubble size and pattern. However, to the best of the knowledge of the author, no work has been done involving pool boiling simulation, using Ansys Fluent, and implementing a VOF sharp interface for a tapered microgap with air injection and boiling setup. Conducting numerical simulations can help to determine the primary factors that affect the behavior of bubbles in tapered conditions. Also, prior research has highlighted the challenges of visualizing the vapor bubbles within a tapered microgap during nucleating pool boiling conditions. Hence, a simulation study involving bubble growth in tapered microgap can serve as a means to identify the hydrodynamic and thermal behavior that leads to lower flow instabilities and higher heat dissipation.

The present study conducts the analysis of bubble growth in tapered microgaps with numerical simulations to identify the effect of the fluid properties and tapered angle in the bubble and fluid dynamics behavior. Ansys-Fluent is customized with user-defined-functions (UDFs) accounting for the interfacial heat and mass transport, including a sharp interface and direct calculation of mass transfer with temperature gradients. The study considered two cases (i) air-injection, (ii) liquid evaporation at the interface. The case of air-injection evaluated the effect of flowrates, working fluid (water, ethanol, and ethylene glycol), tapered angle, and surface tension on the hydrodynamic bubble behavior. The case of liquid evaporation evaluated the effect of multiple nucleation sites on the thermal performance. The results reveal that flowrates and surface tension influence the direction of departure of the bubble. Also, it was identified a suppression in the thermal boundary layer due to fluid circulations near the bubble interface. The following sections describe the work done to conduct the analysis; section 2 gives a brief literature review on multiphase flow simulations, section 3 describes the methods, section 4 illustrates the simulation results, and section 5 states relevant conclusions.

2. Literature review on Numerical Simulations

The literature review focuses on relevant works in numerical simulations of boiling. To better understand the literature, the first section highlights the use of the VOF interface tracking method, second describes the usage of the sharp interface tracking, and the third shows how, 2D simulations agree well with experimental work.

The first part emphasizes identifying the type of simulation and the methods adopted to track the interface. Simulations modify the VOF interface tracking method to properly account for interfacial phenomena such as mass transfer, contact line evaporation, and tracking temperature of mixture cells. Magnini et al. [65] improved VOF interface tracking by implementing a Height Function method to better estimate the local capillary effects and an evaporation model, results indicated that the modified VOF can

capture thin thermal films formed by slug flow. Shipkowski and Perez-Raya [66] proposed an analytical method to accurately compute the interface surface area in multiphase flow modeling, results show that the approach allows a direct estimation of mass transfer with sharp interface, which improves modeling of the heat transfer mechanisms near the interface. Zhao et al. [67] proposed a boundary method that separates the liquid and vapor phases within VOF to accurately compute jump conditions at the interface that allow preservation of the bubble shape and improved agreement with theoretical results. Yeo and Lee [68] experimentally and computationally investigated the subcooled and saturated flow boiling of R-134a in a horizontal heat sink. A good agreement between high-speed images from experimental flow visualization and predicted flow patterns were achieved using the 2D simulation integrating the multiphase VOF method and Lee phase change model where the flow boiling undergoes change from bubbly to annular flow in the micro-channel. Sun et al. [69] used the VOF method and UDF in Ansys-Fluent to improve the accuracy of the 1D Stefan problem, 2D film boiling problem, and condensation. The results showed excellent agreement with experimental data and analytical solutions. Rajendran et al. [70] used open-source VOF solver inter-foam for a two-phase application. They used a modified VOF solver for a suspended droplet in air, jet breakup, drop impact on thin films, and air entrapment during drop interaction with a liquid pool. The modified VOF solver performed significantly better than the original VOF method. Garoosi and Hooman [71] used a modified VOF model to achieve higher sharpness for moving interfaces. They successfully eliminated interface smearing, control the thickness of the interface, preserve the thickness of the interface over 2 to 3 mesh intervals. Fostiropoulos [72] conducted a numerical analysis on the dynamics of fuel oil-water droplets at their interface, using three VOF transport equations. Simulation results revealed that aerodynamic droplet breakup cases shared similar properties and initial conditions with corresponding emulsions. Lin et al. [73] studied the effect of flow boiling in micro-tube geometry using a VOF model to track the interface in divergent, normal, and convergent geometries. A validation against the experimental work in quasi-steady state was achieved, and the results helped understand the effects of micro-tube geometry on flow boiling. Kharangate and Mudawar [74] provide an in-depth review of the VOF method used for simulations involving two-phase flow.

The challenge with VOF methods is to maintain a sharp and well-defined interface between the fluids as it moves and deforms. Sharp interface tracking techniques are employed to achieve this goal. Bureš and Sato [75] carried out a direct numerical simulation for phase change using a sharp-interface algorithm coupled with the diabetic geometric VOF method. Bubble growth in superheated quiescent liquid was simulated using 2D axisymmetric and 3D Cartesian representations with good sharpness and symmetry levels and first-order accuracy. Ménard et al. [76] used a coupled level set-VOF-ghost fluid method to optimize the mass conservation and precise interface characterization, for a 3D simulation of the primary atomization zone of a turbulent liquid jet, and achieved good results. Naghashnejad et al. [77] developed a computational fluid dynamic model to capture the meniscus interface for a capillary flow between vertical parallel plates. The sharp interface tracking and reconstruction could accurately predict the capillary penetration or depression regardless of the wall spacing. An excellent agreement was observed between the numerical predictions and the theoretical solutions for the steady-state capillary height and meniscus shape. Shang et al. [78] used a sharp-interface algebraic VOF model for simulating evaporating droplets, the results showed that the model was able to capture minute details associated with droplet evaporation. Other works have used interface-sharpening equation to prevent smearing of the color function [17], [79]-[81]. Also, it is common to distribute mass source terms into multiple cells around the interface [82]–[86], and employing a split approach for advection of the interfacial mass flux through the faces [87]-[89].

Several mathematical and 2D numerical simulation of bubble growth have shown agreement with experimental results and theoretical models. Numerical work using different fluids, for boiling and condensation, and in superheated region, with various geometrical configurations have shown good results. Dhir et al. [90]-[92] proposed a microlayer modeling approach to simulate boiling and for various operating conditions, including high heat fluxes and microgravity, they observed bubble growth and heat transfer mechanisms. Bardia and Trujillo [93] studied the influence of inertia forces on bubble growth and heat transfer and modeled the effect of pressure on the saturation temperature. Onishi et al. [94] numerically studied a 2D film boiling and condensation problem using the VOF method and validated it against Klimenko's and Nusselt's correlation. The simulation outcome showed that the wall heat flux increases in the presence of working fluid phase change and decreases in higher driving pressure. Çiftçi [95] numerically investigated heat transfer characteristics of kaolin-distilled water and bauxite-distilled water, under saturated boiling conditions using 2D simulation. Transition and film boiling processes were illustrated clearly compared to experimental findings. Lee et al. [96] performed 2D simulation with a VOF model to investigate subcooled nucleate flow boiling of FC-72 for three distinct mass velocities and heat fluxes in vertical upflow. Thorough analysis of velocity and void fraction profiles across the channel demonstrated the effectiveness of the computational model in providing detailed local information. The boiling of LN2 was numerically investigated on a solid and liquid surface using direct numerical simulation of interfacial dynamics using an explicit VOF method by Kumar and Das [97]. The results showed that bubble frequency, diameter, and heat flux in boiling on a solid surface rise linearly as the wall superheat increases. Kamel et al. [98] performed a 2D numerical simulation of pool boiling heat transfer for pure water and silica-based water nanofluid. The authors used user-defined functions (UDF) for surface modification, and the correlation proposed for waiting time showed a good agreement with the experimental data. In a 2D numerical study on density mixing, Rodriguez Ocampo [99] employed an image-based method to assess the accuracy of the results. Qualitative and quantitative analyses of experimental and numerical data revealed comparable outcomes, with globally averaged relative errors ranging from approximately 14% to 19% for different turbulence schemes. Iyer et al. [100] used 2D model created in Ansys Fluent to study the boiling behavior in the receiver of a boiler to improve the performance. The results displayed better understanding of effects of contact angle, heat flux, and accommodation coefficient on the bubble growth, and heat transfer.

The literature shows the importance of using VOF method for modeling multiphase flow to capture the interface and interaction between the fluids. 2D simulations play an important role in understanding complex problems and getting an accurate estimation of the effects of various parameters involved. The current work uses 2D numerical simulation to study the effects of variation of taper angle and flowrates on the evolution and departure of a bubble in a microgap.

3. Methods

The 2D numerical simulation using taper geometry was performed in a customized Ansys 2022 R2 commercial simulation package. The tapered block considers three inclination angles of 5°, 10°, and 15° at flowrates of 3, 15, and 30 ml/min using water as the fluid. The peristaltic pump used in the experimental setup had a capacity to discharge air between the flowrates of 0 to 30 ml/min. Hence, the flowrates were divided into three ranges starting from 3 ml/min to 15 ml/min and 30 ml/min. Ethanol and ethylene glycol are used in automotive engines and industrial cooling systems as coolants. Hence, this study was extended to using ethanol and ethylene glycol with surface tensions 0.022 and 0.047 N/m to compare the departure time of a single bubble with water. Further analysis was done, varying the surface tension between 0.004

to 0.09 N/m and the flowrates between 3 to 30 ml/min. These simulations were carried out to find the critical region to define the flow direction of the bubble. The simulation was run, and bubble shapes were analyzed until a steady bubble growth process was observed. The study was continued further by replacing air injection with a heated surface, using UDFs and a wall superheats of 5 K, with water at atmospheric temperature. Three cases of vapor bubble patched at the convergent end, the divergent end, and with multiple bubble growth was carried out. The following sections describe the computational domain, the boundary conditions, the simulation parameters, and the experimental setup used for validation.

3.1. Computational domain

Figure 1 shows the computational domain consisting of pool of liquid and the tapered block. The domain has length and height of 32 mm and 20 mm. The square tapered block has a dimension of 12 mm and inclination angles of 5° , 10° , and 15° . The initial taper gap from the bottom surface is 1 mm, and the orifice size for air injection is 1 mm. The same computational domain was used for boiling simulation. A water-vapor bubble of 1 mm diameter was patched on bottom surface for boiling simulation. The taper angle was maintained at 5° for the boiling simulation. Table 1 shows additional dimensions of the computational domain. The mesh has a minimum cell size of 40 μ m and a maximum of 50 μ m.

3.2. Boundary conditions

The computational domain enclosure consists of water and air injection from an orifice. Fig. 1 shows the boundary conditions that were used to set up the simulation model in Ansys-Fluent. The mesh grid size is small and uniform in the area of interest, as the study focuses on the bubble growth and departure in and around the tapered microgap. The mesh settings considered a volume split technique to divide the computational domain into the two regions of coarse and fine mesh. In addition, the mesh was uniform by applying a "Face meshing" filter. At the top of the enclosure is pressure outlet. The orifice at the bottom of the enclosure is the velocity inlet. Boundaries that are the left side, right side, and bottom are all defined as walls. Table 1 shows relevant parameters used to define the simulation domain. θ_1 is the leading edge angle for the bubble growing in the tapered microgap. A leading angle refers to the angle formed between the surface of a growing bubble and the solid surface or liquid interface with which it is in contact. This angle directly influences the curvature of the bubble as it expands affecting the pressure and fluid velocities near the bubble edge. It is important to observe that the simulation uses three different taper angles and flowrates. For the boiling simulation, the orifice was replaced by a closed bottom surface that was maintained at 378.15 K, and the saturation temperature of the liquid was 373.15 K.

Parameter	Symbol	Value
Orifice diameter	D	1 [mm]
Domain length	H ₁	32 [mm]
Orifice distance	V ₂	1 [mm]
Taper gap	V_1	1 [mm]
Domain height	H ₂	20 [mm]

Taper length	L _T	12 [mm]
Taper angle	θτ	5°,10°,15°
Leading angle	θ_1	60°
Trailing angle	θ_2	90°
Wall temperature	T _w	378.15 K
Patched bubble diameter	D _b	1 [mm]

TABLE 1: Relevant parameters in the simulation.

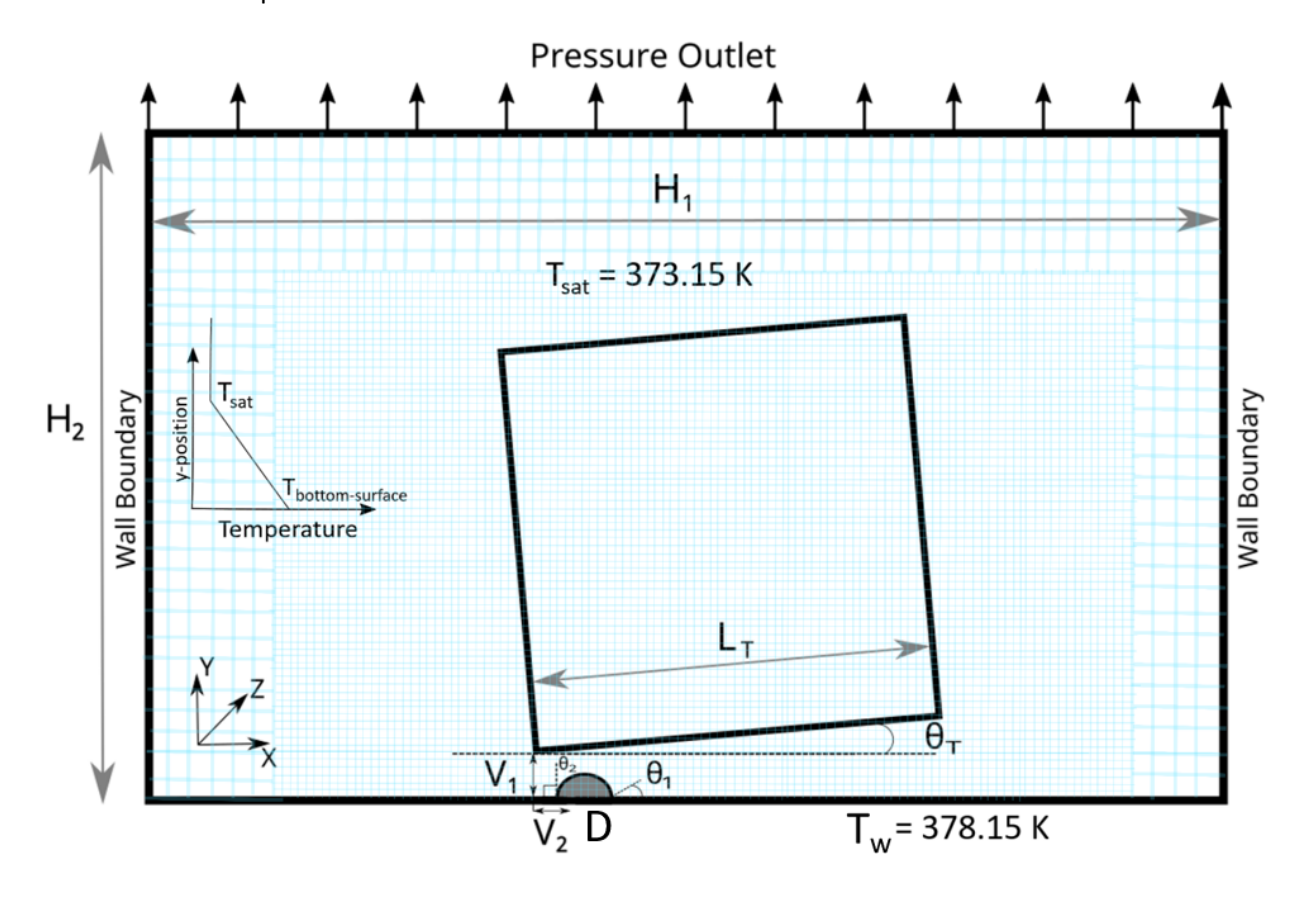


FIGURE 1: Sketch of the computational domain for air injection study, orifice distance is at 1 mm from the convergent end of the tapered block. The orifice inlet has been closed and a bubble of 1 mm diameter is patched for boiling study. The mesh grid size in small and uniform in the area of interest and larger in other areas.

3.3. Simulation settings

The Ansys-Fluent solves the governing equations for continuity, momentum, and volume of fluid. The simulation software solves the volume-of-fluid (VOF) interface tracking equation and uses the sharp interface VOF model. The SIMPLE algorithm was employed to handle the pressure velocity coupling for the air-injection study. Gradient of all flow variables was calculated using the green-gauss cell-based method, while the momentum terms in the governing equation were approximated by the QUICK scheme.

For the boiling simulation, least square cell-based gradient, PRESTO pressure model, and second order upwind momentum model were used. Multiphase model with constant surface tension, wall adhesion to incorporate the leading and the trailing angles for the bubble was used. The Courant number remained below 0.25 in all the simulations to ensure a correct time step size. The Courant number indicates the ratio between the interface displacement and the grid cell size. A Courant number below 0.25 allows the interface to remain within a computational cell for at least four time-steps before moving to the next computational cell, which helps to avoid numerical instabilities. UDF to customize Ansys-Fluent for the boiling simulation were used to track the interfacial interaction of the vapor bubble and the liquid to accommodate mass transfer.

3.4. Governing Equations

The conservation of mass equation is:

$$\nabla \cdot \vec{u} = 0 \tag{1}$$

where ∇ is the gradient operator.

The conservation of momentum equation is:

$$\frac{\partial(\rho\overrightarrow{v})}{\partial t} + \nabla \cdot (\rho \vec{v}\vec{v}) = -\nabla p + \nabla \cdot \{\mu[\nabla \vec{v} + (\nabla \vec{v})^T]\} + F_S + \rho \vec{g}$$
 (2)

where F_S corresponds to the surface tension applied to the cells that have an interface.

The VOF interface tracking equation is:

$$\frac{\partial F_q}{\partial t} + \vec{u}_q \cdot \nabla F_q = 0 \tag{3}$$

where ${\it F_q}$ is the volume fraction of air in the computational cells.

$$\sum_{q=1}^{2} F_q = 1 (4)$$

This constraint will be used to solve for the primary phase since equation (3) does not account for the volume of fractions in the primary phase.

The density and viscosity of the gas and liquid phases are estimated with the volume fractions. The following expressions show the adopted formulation:

$$\rho(\vec{x}, t) = F(\vec{x}, t)\rho_l + [1 - F(\vec{x}, t)]\rho_g$$
 (5)

$$\mu(\vec{x},t) = F(\vec{x},t)\mu_l + [1 - F(\vec{x},t)]\mu_g \tag{6}$$

where ρ is density and μ is viscosity.

Surface tension force is included in the momentum equation using the VOF values that balance the forces at the interface of the two fluids. Equation 7 gives the surface tension force.

$$F_S = \sigma \frac{\rho k \nabla F_1}{0.5 \left(\rho_a + \rho_l\right)} \tag{7}$$

where,

$$k = \nabla \cdot \hat{n} \tag{8}$$

$$n = \nabla F_a \tag{9}$$

The surface tension effect is included, which acts along with the interface between the phases. The surface tension is constant.

Evaporative mass flux:

$$m'' = \frac{k_l \, \partial T}{h_{fg} \, \partial n_{int}} \tag{10}$$

where k_l is the liquid thermal conductivity, h_{fg} is the latent heat of evaporation, and ∂T ∂n_{int} is the temperature gradient at the interface along the normal direction.

The energy conservation equation that provides the temperature for both liquid and vapor phases is given by:

$$\frac{\partial T}{\partial t} + \nabla \cdot \vec{v}T = \nabla \cdot \alpha \nabla T + S_{T}$$
(11)

where α is the thermal diffusivity, and S_T is a source term. The source term fixes the temperature of the interface cells to properly account for the sharp interface. The sharp interface model applies the ghost fluid method and the large coefficients technique to impose the interface thermal condition [101], [102].

The local heat transfer coefficient is given by:

$$h = \frac{-k_l \, \partial T / \partial y|_{y=0}}{T_w - T_S} \tag{12}$$

where, T_w wall temperature, T_s saturation temperature, and k_l wall thermal conductivity.

3.5. Ansys-Fluent customization

To accommodate mass transfer in the simulation without air injection Ansys-Fluent was customized with User-Defined-Function (UDFs). UDFs used temperature gradients at the interface to estimate the mass source term. The UDF "Define-Adjust" was employed to perform several tasks, including identifying the mixture, estimating mass transfer, and setting the temperature of the mixture cells. Source terms in the energy equation were declared by the UDF "Define-Source" to account for the interface saturation temperature. The UDF "Execute-at-the-End" performed a cleaning operation on the variables. OCASIMAT method was adopted to perform the computation of mass transfer and interface cells temperature [103]. The method performs a direct estimation of mass transfer with temperature gradients, imposes the interface saturation temperature, and segregates the mass transfer to preserve the interface sharpness. Perez-Raya and Kandlikar showed validation of the adopted methods with theoretical solutions of planar interface evaporation, spherical bubble growth, and available experiments [104]–[106]. Moreover, the

simulations utilized the analytical method proposed by Shipkowski and Perez-Raya [66] to accurately compute the interface size leading to precise modeling of interfacial heat and mass transfer.

3.6. Experimental setup

The experimental setup consists of a Masterflex L/S peristaltic pump that can pump a fixed air flowrate through a thin tube into a pool of water. The air inlet has a diameter of 1 mm, and the center of this air inlet is located 1 mm from the tapered inlet. The taper inlet gap is 1 mm, and the angle is 5°. The air flowrate was set at 3 ml/min for the experiments, and a Photron high-speed camera was used to record the squeezing air bubble, and the bubble movement was captured at 2000 fps.

4. Results

The results section covers the effect of taper angles, flowrates, surface tension, and heating on the bubble dynamics. The flow was studied using contours of VOF, velocity magnitude, and temperature. Air injection study with single bubble departure is studied first, followed by departure of ten subsequent bubbles. In addition, velocity vectors visualize the fluid interaction with the bubble as it grows and departs. As the flowrate changes, the variation in the flow direction of bubbles is indicated by the departure of additional bubbles. Results from ethanol and ethylene glycol are analyzed to study the effect of surface tension on the bubble departure.

4.1. Mesh analysis

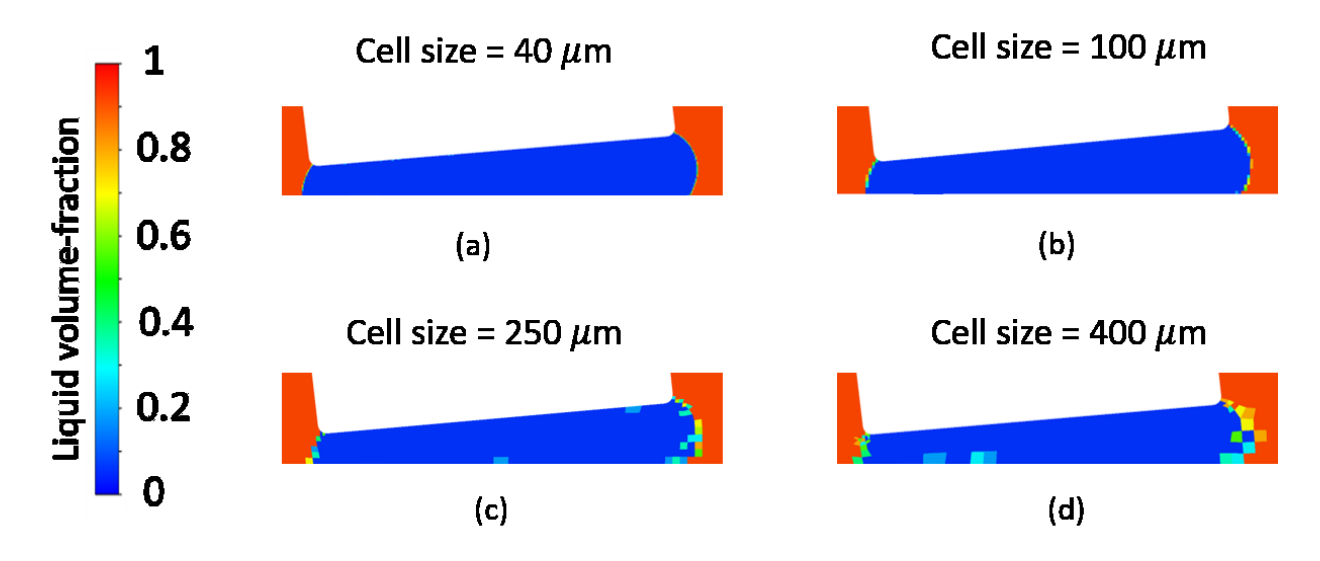


FIGURE 2: Effect of grid cell size on the bubble interface for 5° taper angle at time of 0.80 s. Water and injected air bubble at atmospheric conditions.

The mesh sensitivity test was performed for the case of a 5° tapered angle. Fig. 2 shows the cells at the interface of the bubble generated at time 0.80 s for four grid cell sizes of 40, 100, 250, and 400 μ m. The blue color represents air, the red color represents water, and the interface shows a transition color from blue to red. The results show that the interface resolution shares an inverse relation with the cell size. With the increase in the cell size, the interface tends to degrade further. The cell sizes of a 100 and 40 μ m allow the modeling without interface deformations. We decided to adopt a grid cell size of 40 μ m for all

the studies in the present work due to a good interface resolution and an acceptable number of computational cells.

4.2. Validation of the numerical simulation

Figure 3 compares the different stages of the bubble growth observed in the experiment and simulation. The flowrate is 3 ml/min, and the angle is 5°. The gray color contours on the top show experiments, whereas the bottom side shows the volume fractions, and each figure shows the time on the top. Results indicate a good agreement between the experiment and simulations in terms of bubble shape and behavior. The bubble departs at 0.95 s, according to the experimental data, while the bubble departs at 1.14 s, according to the numerical simulation. The discrepancy between the departure times is 20% which is acceptable. The difference might be due to the 3D experiment effects that were ignored by the simulation.

The numerical results in Fig. 3 show the evolution of a bubble in a tapered microgap at an inclination angle of 5°. The important factors to take into consideration are time of departure, the bubble shape, and direction of departure between the simulation and the experimental results. The figure shows five different time frames selected to illustrate the bubble shape from conception to departure. At the time of 0.02 s, the bubble is still growing and is not yet in contact with the tapered block. The bubble growth rate, the bubble shape match well with the experimental results. At a time equal to 0.75 s, the bubble continues to grow due to constant injection of air and creates a slug once it is in contact with the taper and keeps moving forward in the right direction towards the diverging end. This movement of the bubble towards the divergent end as well as the slug shape matches well with the experimental results. At t = 0.98 s, the bubble has completely covered the taper area and is still moving towards the diverging zone. At time t = 1.06 s, the bubble forms a neck at the edge of the taper and looks set to depart. This neck formation and bubble detachment is in good agreement with the experimental result. The bubble fully leaves the tapered surface at 1.14s. Throughout the process of bubble formation, movement towards divergent end, and departure, the bubble maintains a good curvature along the interface similar to experimental result and does not smear or changes shape conforming to the usage of VOF and sharp interface.

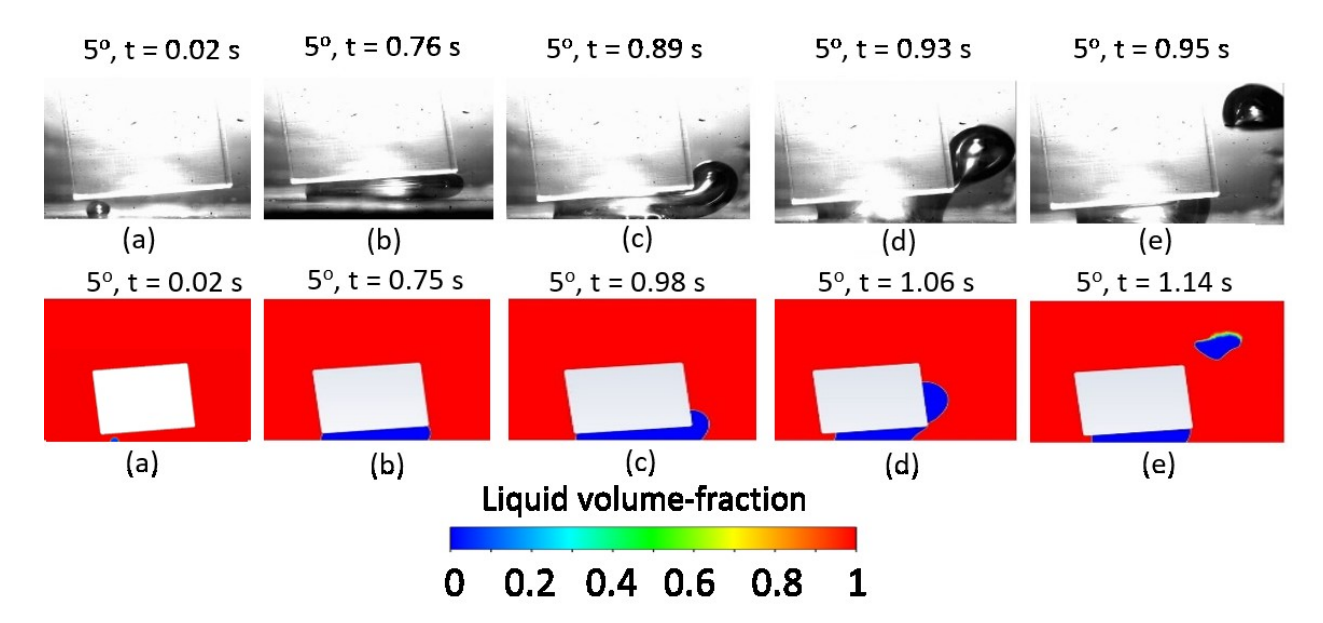


FIGURE 3: Validation of the numerical model for bubble growth at 5° taper angle against the experimental results. Water and injected air bubble at atmospheric conditions.

Figure 4 shows the velocity vector of the 5° case. The velocity vectors are displayed in color with the magnitude varying from blue to red (low to high), the air bubble in black color, and the taper block in white. Initially, the bubble formation indicates the velocity vectors of maximum magnitude pushing the liquid toward the convergent side. As the bubble grows, the surface tension and the leading edge angle move the bubble toward the divergent end. At time 0.75 s, the bubble continues to grow due to constant injection of air and creates a slug once it is in contact with the taper and forces the liquid under the taper outwards which can be seen in Fig. (b). At time 0.98 s, the velocity vectors create a circular motion forcing the liquid to move in the lower section of the leading edge of the bubble, which leads to bubble moving towards the upper section of the divergent end. The change in direction eventually leads to a decrease in the velocity magnitude at the convergent end. The bubble can be seen separating at time 1.06 s, where the velocity vectors at the leading edge are pushing the liquid away, while the trailing edge sees the velocity vectors of higher magnitude helping in the separation of the bubble from the bigger volume of bubble. Once the bubble departs from the tapered microgap at 1.14 s, high fluid circulation can be observed around the bubble due to sudden change caused by detachment and departure. Fluid of higher magnitude, compared to previous time sets, can be seen at the convergent end pushing the remaining volume of the bubble, which should ensure departure of the bubble at the divergent end for the case of 5° and flowrate of 3 ml/min.

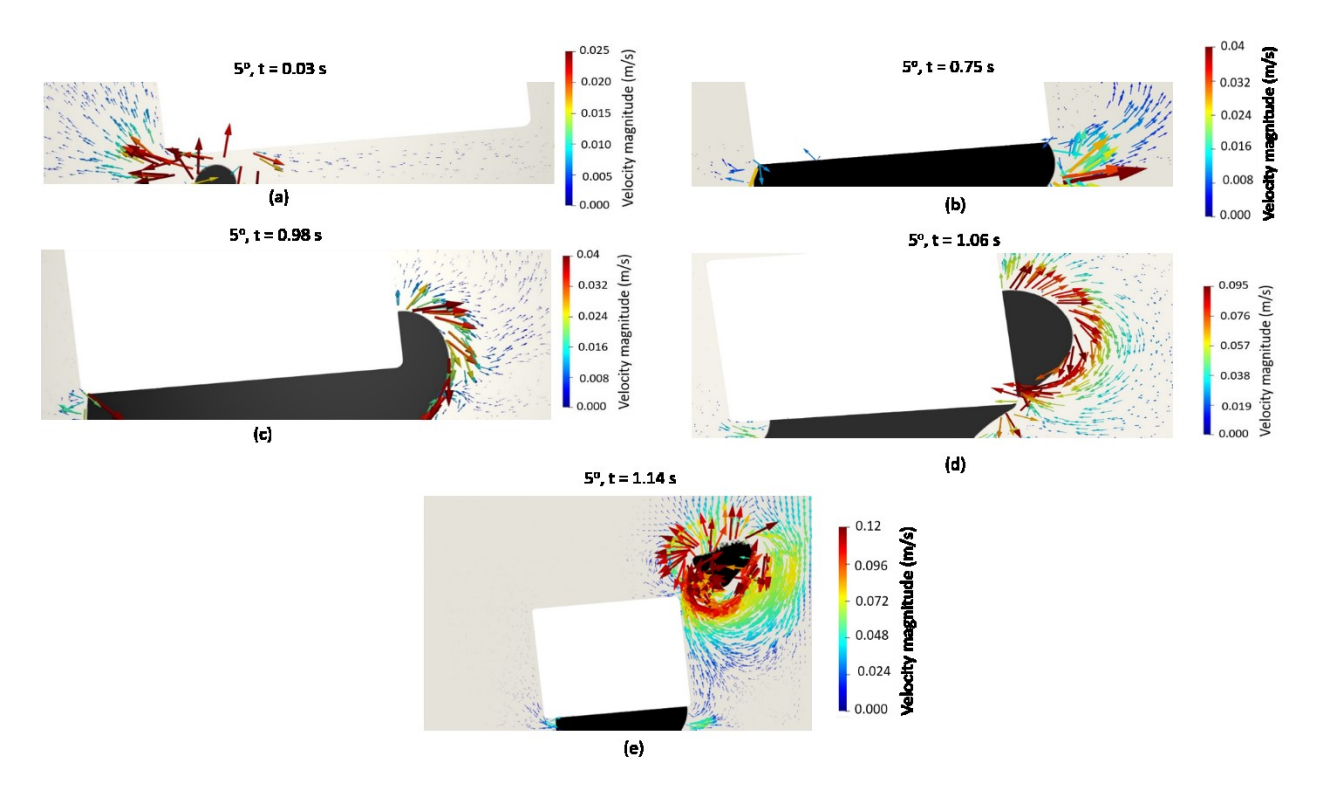


FIGURE 4: Velocity vectors of 5° taper angle for bubble growth at three different time instances of 0.03 s, 0.98 s, and 1.06 s. Water and injected air bubble at atmospheric conditions.

4.3. Effect of the tapered angle on bubble dynamics

Figure 5 shows the growth and departure of the first bubble at an inclination angle of 10° with water as working fluid. The figure shows six different time frames selected to illustrate the time from the conception of the bubble to its departure. At t = 0.06 s, the bubble shows a similar pattern of growth relative to the 5° degree tapered angle case. Also, at the time of 0.608 s, it can be seen that the bubble continues to grow, and it goes through a squeezing effect between the taper and the bottom surface. The bubble then moves towards the diverging edge of the tapered microgap. The bubble forms a similar neck pattern as that of the 5° case. The detached bubble seen at t = 1.38 s leaves the tapered surface entirely at 1.44 s. The results of the simulation show a larger time of departure in the 10° relative to the 5° case due to the increase in flow area with a higher angle.

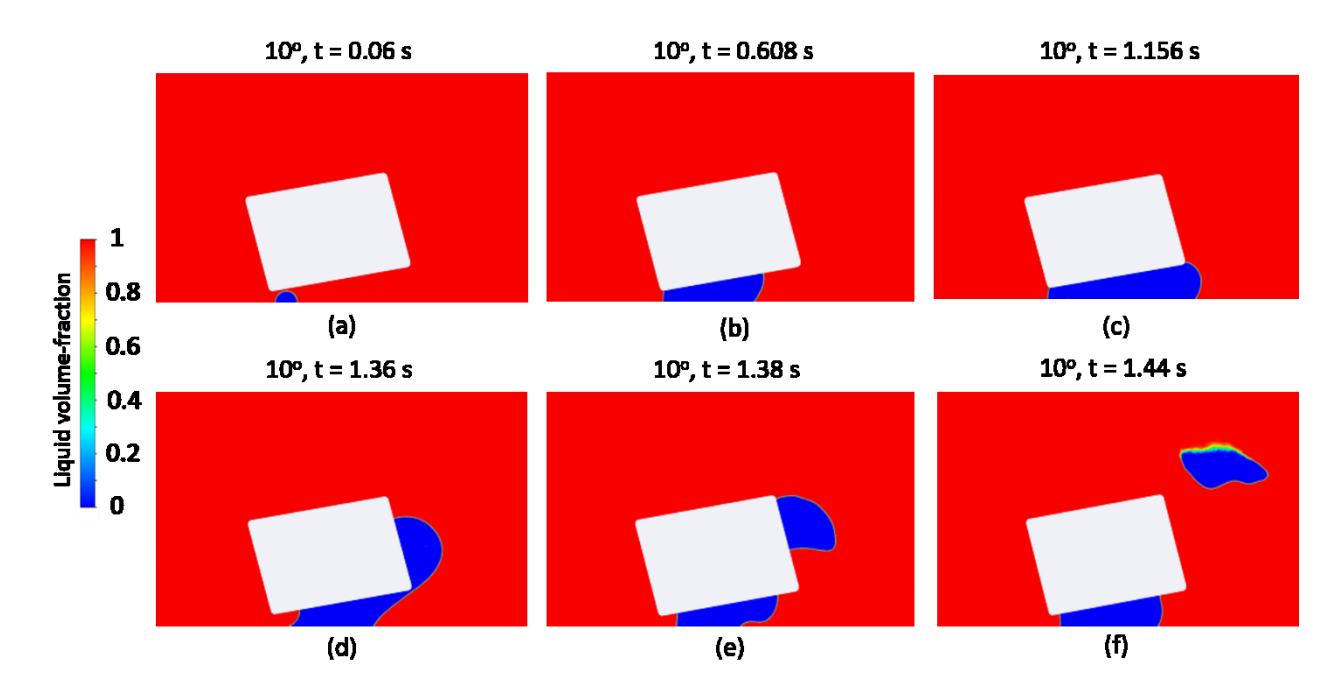


FIGURE 5: Growth and departure of the first bubble for taper angle $\theta_T = 10^\circ$. Water and injected air bubble at atmospheric conditions.

Figure 6 shows the growth and departure of the first bubble at an inclination angle of 15° . At t = 0.06 s, the bubble is still far from the tapered surface. Similar to previous cases, when the bubble comes in contact with the tapered surface at t = 1.40 s, the bubble moves towards the divergent end. The time for the bubble to reach the divergent edge of the taper is relatively higher compared to the previous cases. This can be attributed to the more area available for the bubble to expand at the same flowrate. The volume of the bubble, as it moves to the right, becomes more prominent, creating a more extended interface between the liquid and air. Eventually, the bubble grows large enough and can neck and depart the microgap, which can be seen from t = 1.74 s to t = 1.79 s. The results of the simulation illustrate that even with a high tapered angle of 15° , the bubble still moves toward the divergent end of the tapered channel.

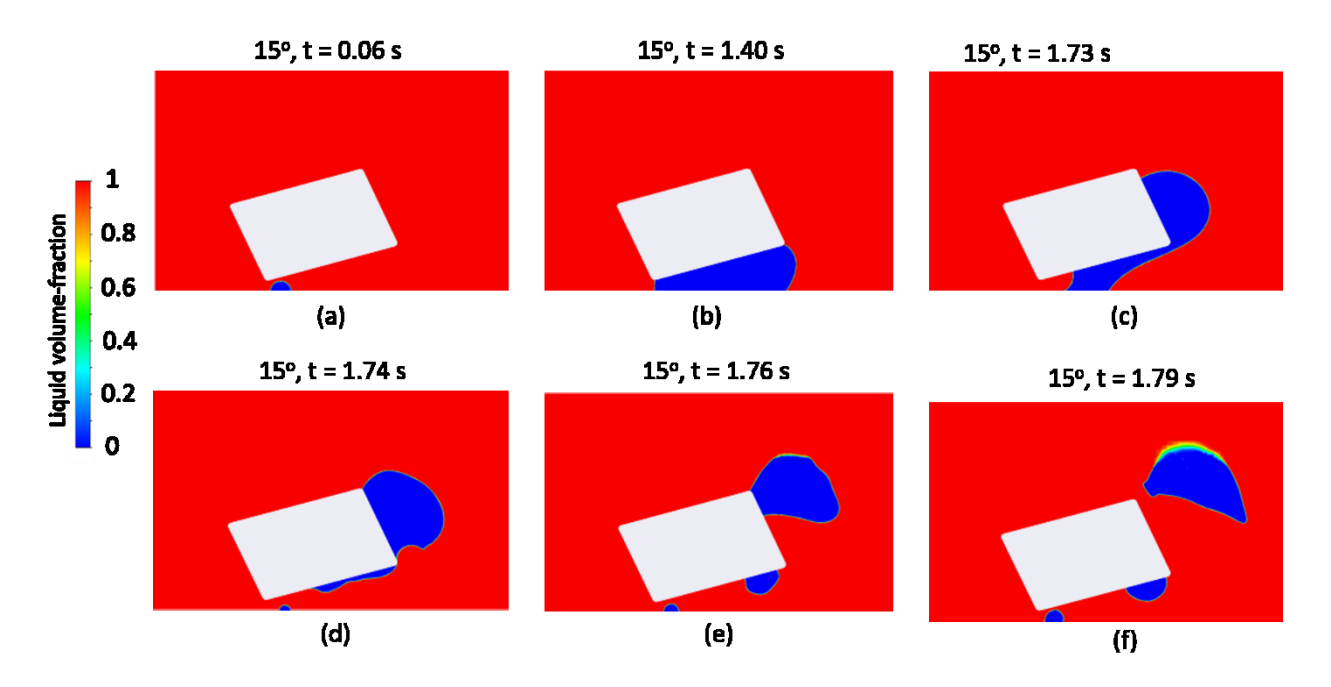


FIGURE 6: Growth and departure of the first bubble for taper angle $\theta_T = 15^{\circ}$. Water and injected air bubble at atmospheric conditions.

4.4. Direction of bubble departure

To study the effects of the flowrates, departure of ten subsequent bubbles were simulated for three flowrates of 3, 15, and 30 ml/min at the three angles of 5°, 10°, and 15°. Tables 2, 3, and 4 show the direction of bubble escape for each analyzed case. Letter C stands for convergent and D stands for divergent, symbolizing the direction of bubble departure at convergent and divergent ends of the tapered geometry. The time of bubble departure followed by the direction of departure is mentioned in the columns of the bubble number.

Departure of ten subsequent bubbles for each flowrates have been reported in Tables 2, 3, and 4 for analysis. This study focuses on the direction and time of departure of bubble for the three analyzed flowrates. Table 2 (flowrate of 3 ml/min) shows bubbles escaping only in the divergent end (D) of the taper. Table 3 (flowrate of 15 ml/min) shows cases for which the direction of bubble departure is unpredictable. Table 4 (flowrate of 30 ml/min) displays the case where the bubbles only depart in the convergent end (C). The first bubble for the 3 ml/min case and angles 5°, 10°, and 15° all escape at the divergent end. For the case of 15 ml/min and 5° tapered angle, the first bubble moves to the convergent end, while for 10° and 15° cases, the first bubble moves towards the divergent end. Compared to each case, the quickest departure of the bubbles can be seen for the 5° taper angle with a flowrate of 30 ml/min. In each of the cases of 3 ml/min and 30 ml/min, the unidirectional departure of the bubble prevents it from causing a backflow condition. The case with a flowrate of 15 ml/min is a mix of the other two cases. The bubble escapes on either end without a particular pattern and has no cyclic pattern.

No. $ heta_T$	1 st	2 nd	3 rd	4 th	5 th	6 th	7 th	8 th	9 th	10 th
5°	1.13 s	0.47 s	0.47 s	0.47 s	0.48 s	0.47 s	0.47 s	0.48 s	0.05 s	0.92 s
	(D)									
10°	1.44 s	0.73 s	0.75 s	0.74 s	0.74 s	0.74 s	0.73 s	0.74 s	0.73 s	0.73 s
	(D)									
15°	1.79 s	1.52 s	1.49 s	1.47 s	1.43 s	1.41 s	1.39 s	1.3 s	1.4 s	1.3 s
	(D)									

TABLE 2: Direction of departure of first 10 bubbles for the flowrate of 3 ml/min. (D) indicates bubble moving to the divergent end of the channel. The number indicates the departure time from the previous bubble in seconds (s) it takes for the bubble to depart. Water and injected air bubble at atmospheric conditions.

Results in Table 2, 3, and 4 for the flowrates of 3 ml/min, 15 ml/min, and 30 ml/min show that the time of departure of a bubble increases with the increase in the angle. 15° tapered angle always has the highest departure time for every bubble from the 1st to the 10th. As the flowrate increases, the highest departure time of the bubbles, i.e., for the 15° tapered angle, is lower than the 5° tapered angle of the previous case of lower flowrate. The bubble departure time, on average, decreased by 1.2 seconds when compared between the cases of 5° of 3 ml/min and 15° of 15 ml/min, and it decreased by an average of 0.2 seconds when compared between the cases of 5° of 15 ml/min and 15° of 30 ml/min. These comparisons further exemplify that the departure time of the 15° tapered angle moves closer and closer to the 5° tapered angle case as the flowrate increases.

Bubble No. $ heta_T$	1 st	2 nd	3 rd	4 th	5 th	6 th	7 th	8 th	9 th	10 th
5°	0.31 s	0.23 s	0.11 s	0.19 s	0.2 s	0.22 s	0.14 s	0.12 s	0.14 s	0.12 s
	(C)	(D)	(D)	(C)	(C)	(D)	(D)	(D)	(D)	(D)
10°	0.4 s	0.23 s	0.15 s	0.29 s	0.21 s	0.12 s	0.32 s	0.23 s	0.14 s	0.23 s
	(D)	(C)	(D)	(D)	(C)	(C)	(D)	(C)	(C)	(C)
15°	0.47 s	0.37 s	0.4 s	0.36 s	0.33 s	0.39 s	0.21 s	0.46 s	0.12 s	0.42 s
	(D)	(D)	(D)	(D)	(C)	(D)	(C)	(D)	(C)	(D)

TABLE 3: Direction of departure of first 10 bubbles for the flowrate of 15 ml/min. (C) and (D) indicates the bubble moving to the convergent and the divergent ends of the channel. The number indicates the

departure time from the previous bubble in seconds (s) it takes for the bubble to depart. Water and injected air bubble at atmospheric conditions.

In addition, results in Table 2, 3, and 4 show that in 3 ml/min, the bubble grows in the divergent end of the taper, which causes bubble squeezing, further increasing the bubble departure time. The bubbles travel the whole length of the tapered geometry before it reaches the edge, where the circulating forces of the liquid help break the bubble from the trailing volume and escape the surface. This is not the case for the bubbles departing at a flowrate of 30 ml/min. The bubbles grow under the taper but quickly move towards the convergent end, thus saving time by preventing them from growing under the longer side of the taper. Also, the volume of the departing bubble increases with the increase in tapered angle for the case of 3 ml/min. Another important observation made was the direction of departure of bubbles for the angles of 10° and 15° that are similar to the case of 5°. For the flowrate of 3 ml/min, all the bubbles for 5° depart at the divergent end, and the same can be seen for the angles of 10° and 15°. Similarly, for the flowrate of 30 ml/min, the bubbles depart at the convergent end for 5°, and a similar pattern is seen for 10° and 15° tapered angles. For the flowrate of 15 ml/min and 5° tapered angle, bubble departure does not have a particular direction, and although not identical, the 10° and 15° cases face the same issue. And thus, it can be established that the 5° tapered angle can be used as the base case for further analysis.

Bubble No. $oldsymbol{ heta}_T$	1 st	2 nd	3 rd	4 th	5 th	6 th	7 th	8 th	9 th	10 th
5°	0.19 s	0.07 s	0.13 s	0.09 s	0.1 s	0.1 s	0.1 s	0.1 s	0.1 s	0.1 s
	(C)									
10°	0.21 s	0.09 s	0.1 s	0.1 s	0.11 s	0.09 s	0.11 s	0.1 s	0.1 s	0.1 s
	(C)									
15°	0.22 s	0.15 s	0.18 s	0.07 s	0.19 s	0.13 s	0.17 s	0.18 s	0.12 s	0.16 s
	(C)									

TABLE 4: Direction of departure of first 10 bubbles for the flowrate of 30 ml/min. (C) indicates a bubble moving to the convergent end of the channel. The number indicates the departure time from the previous bubble in seconds (s) it takes for the bubble to depart. Water and injected air bubbles at atmospheric conditions.

It can be seen in table 5 that for the first column, the time of departure for the 15° tapered angle at 3 ml/min is the highest because of the huge volume of the bubble that grows in the tapered microgap, taking significant time. But for the case of 15 ml/min, the bubble departure takes place in either of the ends of the tapered microgap. This significantly brings down the average time taken for bubbles to depart, as some of the bubble depart at the convergent end, where they do not travel the length of the tapered microgap, while few bubbles exit at the divergent end traveling the length of the microgap. Thus, in the second column, the average time of departure is comparatively lower than column one. For the third column, the flowrate is 30 ml/min where all the bubbles depart only in the convergent end, and thus, the average time of departure is lower than the other two columns for all the tapered angles.

Flowrate $ heta_T$	3 ml/min	15 ml/min	30 ml/min
5°	0.475 s	0.163 s	0.098 s
10°	0.736 s	0.210 s	0.100 s
15°	1.410 s	0.340 s	0.150 s

TABLE 5: Overall average bubble departure time for 2nd to 10th bubbles for each flowrate and tapered angles.

4.5. Effect of the fluid with ethylene glycol and ethanol

Ethylene glycol and ethanol were used as fluids to evaluate the effect of surface tension on the departure time of the bubble. Table 6 shows the different fluids and the corresponding properties considered in the simulation with air-injection. The reported saturation temperature in the table corresponds to atmospheric pressure conditions. Water is a common working fluid in heat transfer systems. Ethylene glycol has higher boiling point compared to water and it is widely used as additive as an anti-freeze in heat transfer applications. Ethanol has a lower boiling point which makes it applicable for electronics cooling. Ethanol and ethylene glycol have good dielectric strengths. Table 7 shows the time of departure for the three different fluids. Results show that for the same boundary conditions and a flowrate of 3 ml/min, the time of departure for water was highest compared to the other two fluids. This can be attributed to the fact that water has surface tension of 0.072 N/m which is higher than 0.047 and 0.022 N/m of ethylene glycol and ethanol. As the surface tension decreases the departure time decreases as well, hence, surface tension seems to be directly proportional to the time of departure of the bubble. The time of departure of the bubble increases with the increase in the tapered angle in all cases. Although other fluid properties affect the overall departure time, surface tension does seem like an important parameter affecting the growth and departure of a bubble. Surface tension forces act along the curvature of the bubble, which impacts the shape and size of the bubble.

Fluid	Surface Tension	Density	Viscosity	Saturation	
	(N/m)	(kg/m³)	(kg/ms)	Temperature (°C)	
Water	0.072	998.2	0.001003	100	
Ethylene Glycol	0.047	1111.4	0.0157	198	
Ethanol	0.022	790	0.0012	78	

TABLE 6: Properties of the three fluids used in simulation for analyzing the effects of surface tension.

Fluid	5°	10°	15°
Water	1.14 s	1.44 s	1.79 s
Ethylene glycol	1.07 s	1.37 s	1.64 s
Ethanol	1.00 s	1.26 s	1.38 s

TABLE 7: Time of departure of the 1st bubble for the three analyzed fluids, at all the three angles of inclination, with a flowrate of 3 ml/min.

4.6. Effect of surface tension

Working with different fluids (water, ethanol, and ethylene glycol) provided insights that surface tension plays and important role in the growth and direction of departure of the bubble. The study was further extended to find a zone for different surface tension values that would impact the direction of departure of the bubble. To find that out, we used water as the fluid, where all the other properties remained the same, while the surface tension was varied between 0.004 to 0.09 N/m. This study further evaluates the capabilities of Ansys-Fluent to simulate the whole range of variation in the surface tension values. Although we understand that such fluid might not exist in real applications, but understanding the impact of surface tension was of importance to us.

To carry out this study a flowrate of 3 ml/min for a 5° taper angle was kept constant, with water and air (with an adjusted surface tension) as fluids. The surface tension varied between 0.004 N/m to 0.09 N/m. As seen in Fig. 7, results of the simulation showed that the bubbles only depart at the convergent end for the surface tension value of 0.007 N/m. At surface tension of 0.007 N/m, the bubble breaks down easily at the convergent end from the bigger volume and escapes. This establishes 0.007 N/m as the critical value impacting bubble escape direction. All the surface tension values between 0.004 N/m and 0.007 N/m, showed bubbles departing at the divergent end. For $\sigma > 0.007$ N/m, the bubble would grow either in the convergent or divergent end. Thus, the value of 0.008 N/m which is just after 0.007 N/m was mentioned to showcase the beginning of the transition region where bubbles will depart in either of the convergent of the divergent ends However, the simulation revealed that with $\sigma = 0.03$ N/m bubbles escape only at the divergent end. Surface tension in the range of 0.007 < σ < 0.03 N/m act as the transition region where the direction of the bubble departure is not fixed. For $\sigma > 0.03$ N/m the bubbles only escape in the divergent end. The surface tension value of 0.022 N/m is one of the values in the transition range and hence was mentioned to show the wide range of the transition region. This also helps establish that surface tension forces impact the flow direction of the bubble. As the bubble grows it experiences momentum force due to the velocity of air injection and surface tension forces along the curvature of the bubble. The balance between these two forces highly influences the direction of the bubble departure. This may be due to momentum forces becoming more dominant than the surface tension forces, leading to the departure of the bubble.

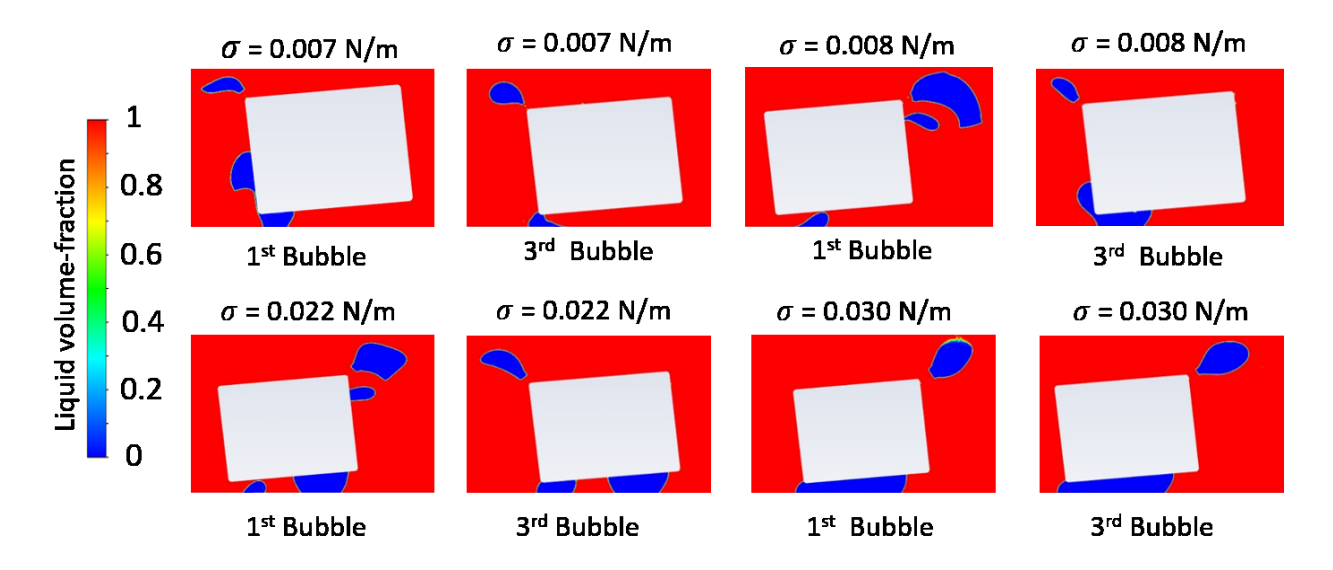


FIGURE 7: Effect of surface tension on the direction of departure of the first and the third bubble at a flowrate of 3 ml/min.

Figure 8 shows the computed variation of the pressure difference from the trailing to the leading edge for different surface tension values ($\Delta P = P_{leading} - P_{trailing}$). Such a pressure difference is one of the driving factors causing the bubble to depart from the divergent end [107]. The pressure difference was calculated from the numerical simulation results when after the bubble reaches the top surface of the tapered microgap. Results show that as the surface tension directly affects the pressure difference. When σ = 0.007 N/m (before the transition region), the pressure difference is already too low and the bubble depart from the converging end. Raghupathi and Kandlikar [108] present a theoretical model explaining asymmetric bubble trajectory by making a force balance accounting for the various interfacial forces including the evaporation momentum force [109].

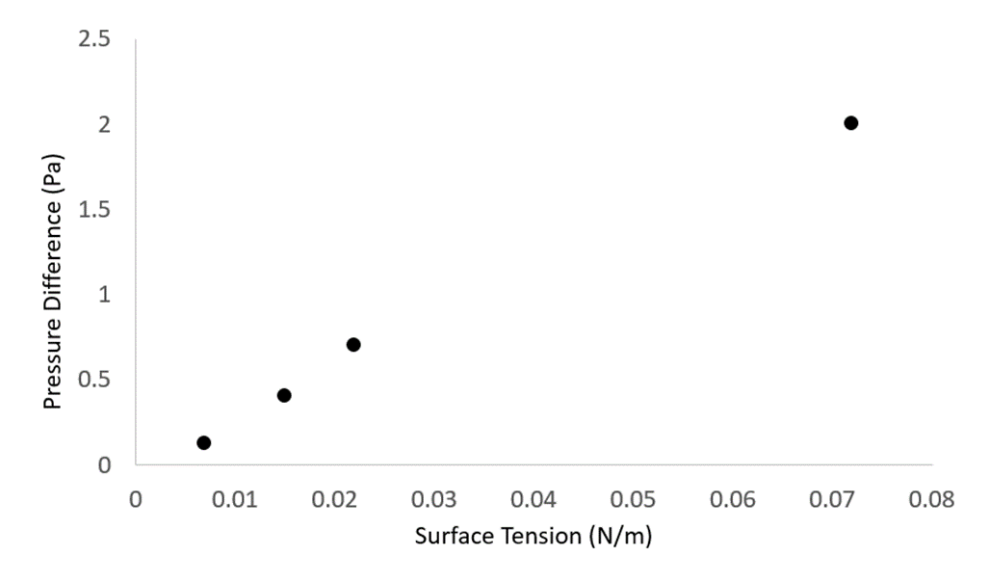


FIGURE 8: Effect of surface tension on the pressure difference between the leading and trailing edge of the bubble at a flowrate of 3 ml/min.

4.7. Effect of flowrate

Numerical simulation were also employed to evaluate the effect of the injected mass flowrate. The range between 3 ml/min and 30 ml/min was divided into multiple flowrates to find the critical value where the bubble escape route changes from divergent end to convergent end. Throughout this study, the surface tension was maintained at 0.072 N/m with air and water as working fluids. The analyzed flowrates, Q_l , were 3, 4, 15, 20, and 25 ml/min. Fig. 9 depicts the results of the simulation for the first and third bubble. $Q_l > 3$ ml/min showed uncertainty in the direction of bubble escape. A flowrate in the range of 3 < $Q_l <$ 20 ml/min show a change in the bubble departure. At the flowrate of 4 ml/min, the direction of bubble escape becomes unpredictable as bubbles escape in both directions. At $Q_l > 20$ ml/min the direction of the bubble escape becomes constant again in the convergent section. With the increased dominance of the momentum forces (coming from the higher flowrates), the ease of escape for the bubble becomes a factor that influences the movement of the bubble. As the bubble grows closer to the convergent end, it is expected to grow and squeeze under the tapered block, and the increased diameter along the length helps it move toward the divergent end. But when the flowrate increases, the bubble does not get enough time to grow along the length of the tapered block. The bubble grows past the convergent end, finding an easier means of growth without a restricting geometry along the vertical-axis. The subsequent bubbles are affected by the sudden detachment leading to the trailing volume undergoing to-and-fro motion. When the bubble experiences an increased to-and-fro motion along with the increased momentum forces, it tends to change the direction of growth. The ease of growth of the bubble, along with the increased momentum forces, creates instability in the system until the bubble only escapes at the convergent end.

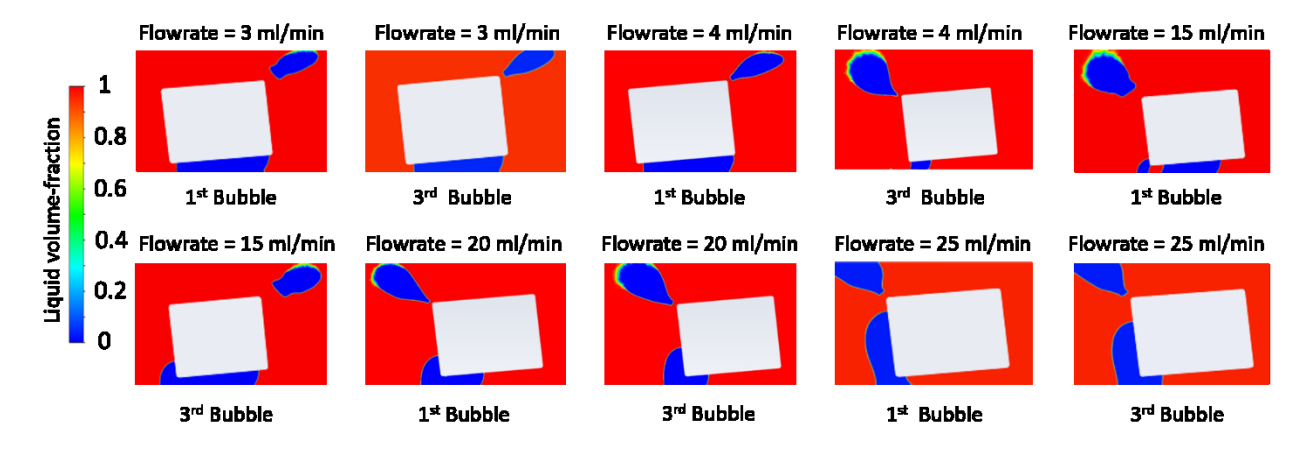


FIGURE 9: Effect of air-injection flowrate on the direction of departure of the first and the third bubble at a surface tension of 0.072 N/m. Water and injected air bubble at atmospheric conditions.

4.8. Heat transfer modeling

Simulations with a vapor bubble growing due to evaporation at the interface was conducted to evaluate the effect of the tapered microgap on the heat transfer characteristics. The bottom wall surface had a temperature of 378.15 K and initially the liquid is assumed to be superheated with a linear temperature profile changing from 378.15 K at the surface to 373 K at 1 mm from the surface. The leading and trailing angles of the bubbles were kept at default values which fluent assigns as we were interested in checking

if we could see a bubble grow under the tapered geometry. Fig. 10 shows the results of the simulation for the volume fraction contours of the first bubble. Since evaporation takes place at the interface without air injection, the first bubble's departure time varies significantly compared to the air injection case with a 5° tapered angle. As seen in Fig. 10, the patched bubble is of 0.5 mm radius, bubble growth is similar to air injection simulations, where the bubble grows and moves towards the divergent end due to the bubble squeezing between the taper and the bottom surface.

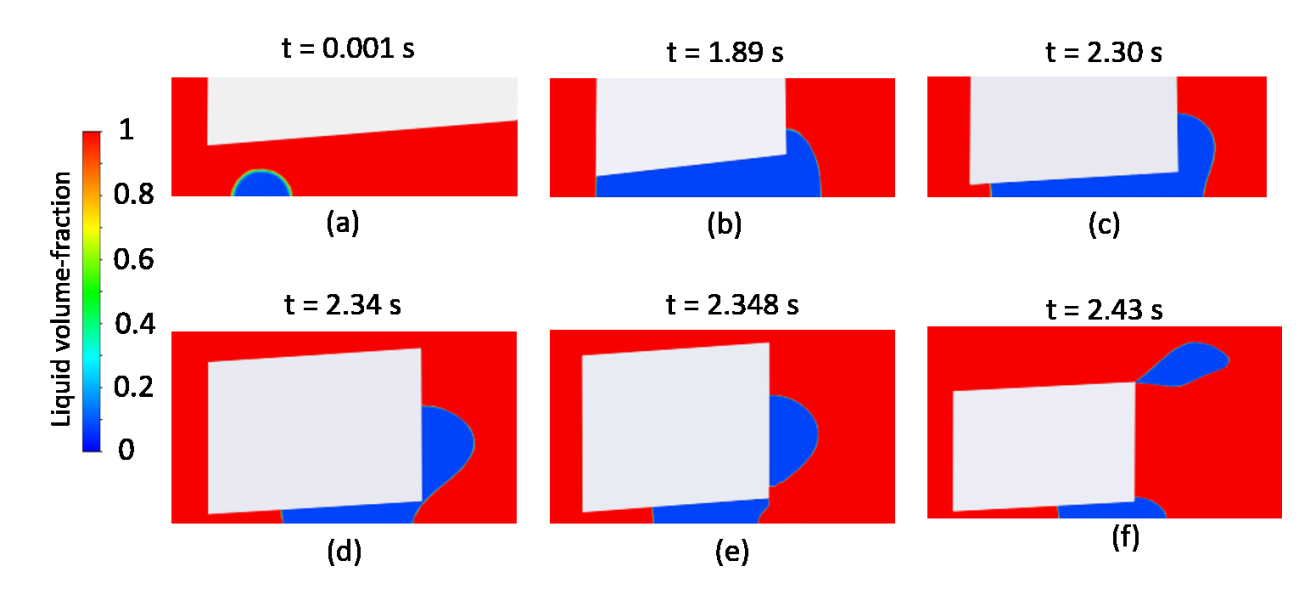


FIGURE 10: Growth and departure of an air bubble at $T_w = 378.15$ K, for a taper angle of 5°, in water at atmospheric conditions. No air injection, bubble grows from liquid evaporation at the interface.

A visualization of the temperature change is seen in Fig. 11. The color red shows $T_w = 378.15$ K and the colors gradually change to dark blue which shows $T_{sat} = 373.15$ K. Fig. 11(a) and (b) shows the bubble growing and, due to the squeezing effect, moving towards the divergent end. Fig. 11(c), (d), and (e) displays cold liquid moving under the taper geometry while the bubble escapes at the divergent end, which leads to thermal layer squeezing. Convective heat transfer is evident when we compare Fig. 11(a), where the heated red contours are close to the bubble, while in Fig. 11(c), and (d), the colder fluid, shades of blue contours, surround the bottom layer of the bubble. Fig. 11(e), and (f) show the recirculation of cold fluid as the bubble breaks at the edge of the taper and escapes. Once the bubble escapes, the observed fluid circulation under the taper geometry is similar to that of air injection. The circulating cold fluid seems to push the bubble from the trailing edge while covering the heated surface and aiding with the heat transfer leading to a temperature drop on the heated surface.

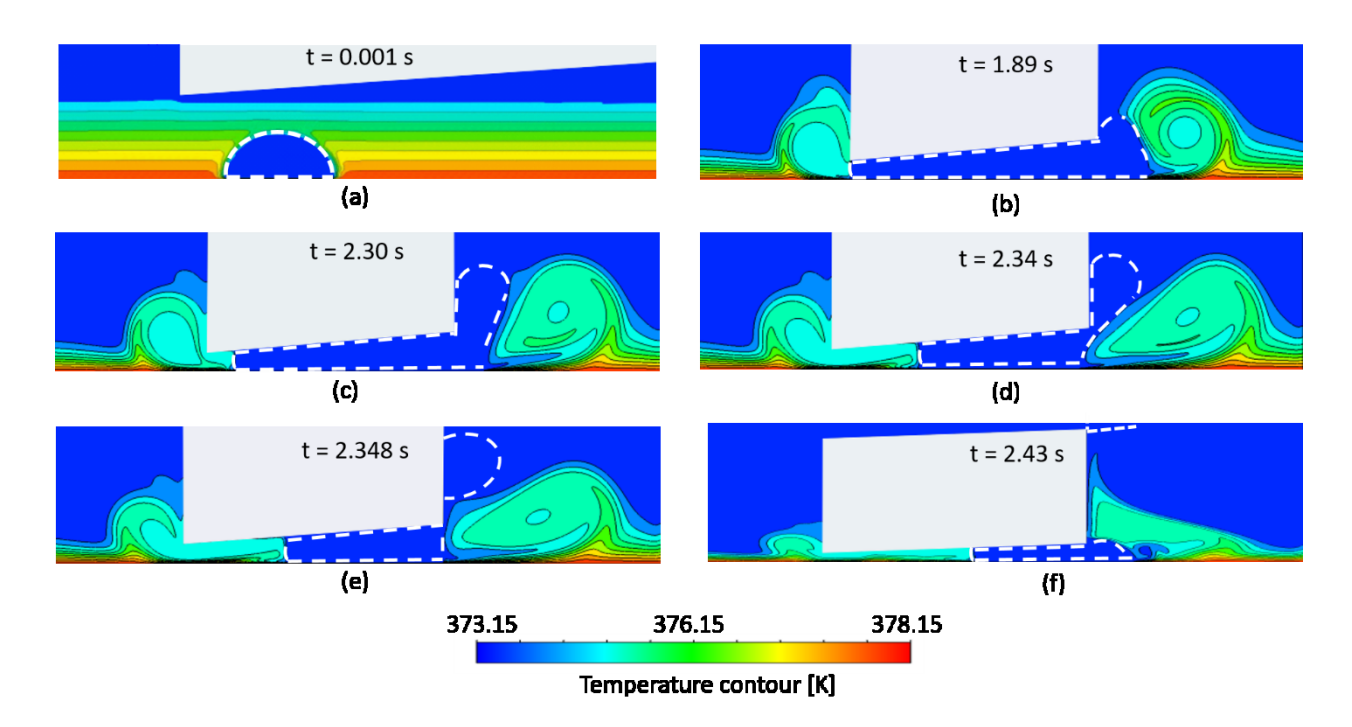


FIGURE 11: Temperature contours of boiling simulation showing growth of vapor bubble (marked with white boundary) in water at atmospheric conditions, fluid recirculation, and suppression of thermal boundary layer for a taper angle of 5°. No air injection, bubble grows from liquid evaporation at the interface.

Figure 12 shows the growth of a 0.5 mm radius vapor bubble patched at the divergent end of the tapered microgap. The bottom wall surface had a temperature of 378.15 K and initially the liquid is assumed to be superheated with a linear temperature profile changing from 378.15 K at the surface to 373 K at 1 mm from the surface. Initially, the vapor bubble undergoes growth, and upon reaching the tapered block, it initiates movement towards the convergent end while continuing to expand. Eventually, the bubble fully develops from the convergent end, showcasing that the bubble tends to migrate towards and grow at the convergent end. This observation provides justification for the bubble patching at the convergent end. Fig. 11(a) to (e) shows the squeezing of the thermal layer due to the growth and movement of the bubble as well as fluid circulations, leading to temperature drop at the heated surface. Fig. 12(f) and Fig. 11(b) have a similar profile of the vapor bubble at the edge of the divergent end of the tapered block, and approximately similar time, which shows that the vapor bubble accelerates while it moves towards the convergent end, causing higher mixing of the liquid, evident in the temperature contour at the two ends of the tapered block.

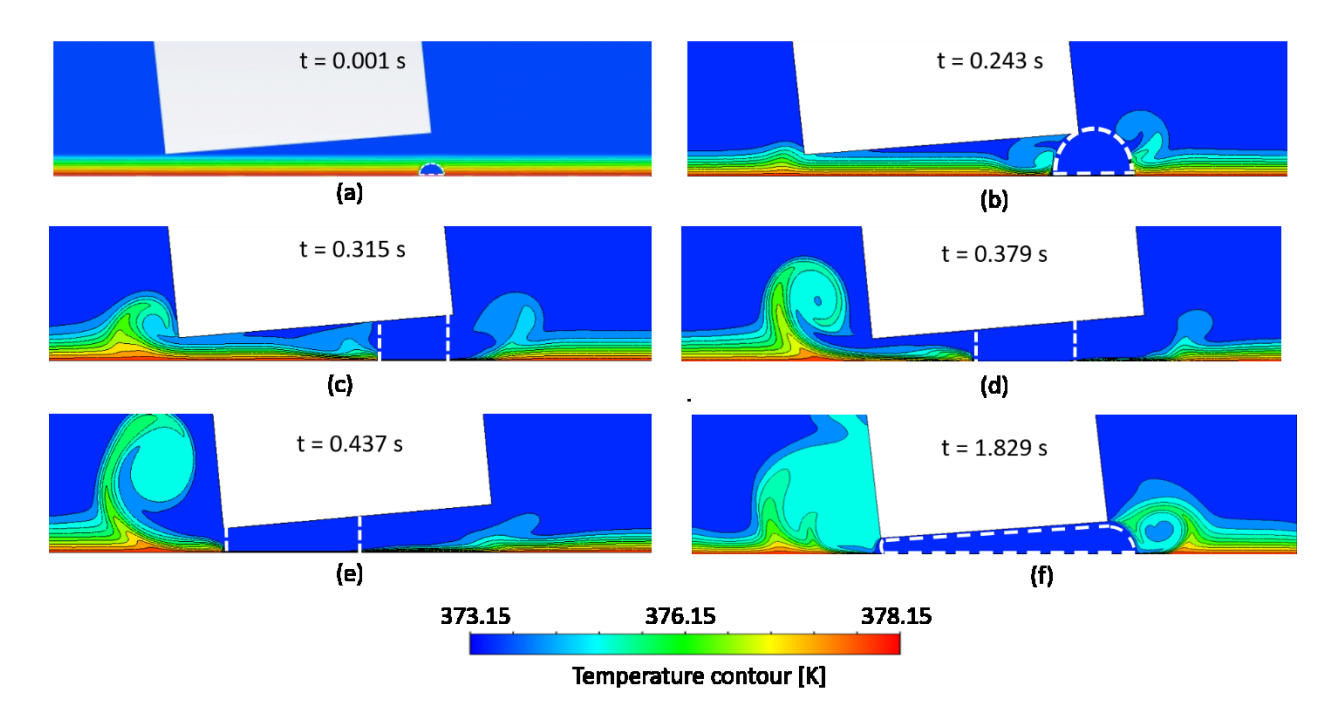


FIGURE 12: Temperature contours of boiling simulation showing growth of vapor bubble (marked with white dotted boundaries) in water at divergent end, fluid recirculation, and suppression of thermal boundary layer for a taper angle of 5°. No air injection, bubble grows from liquid evaporation at the interface.

The previous result showed that the patching of the bubble at the convergent end works well, and hence the study was carried forward to check the impact of multiple bubble growth. Fig. 13 shows the growth of three vapor bubbles each of 0.5 mm radius, patched at a distance of 1 mm apart, starting from 1 mm distance from the convergent end. The bottom wall surface had a temperature of 378.15 K and initially the liquid is assumed to be superheated with a linear temperature profile changing from 378.15 K at the surface to 373 K at 1 mm from the surface. We can see the three vapor bubbles patched together in Fig. 13(a), and as they grow the second bubble from the left merges with the third bubble and they grow together, creating two separate entities, with liquid entrapped between them. Fig. 13(b) shows the two vapor bubble growing and moving towards the divergent end, and the thermal layer between them being ruptured. The leading bubble grows, and departs leaving behind a small volume of vapor seen in Fig. 13 (d). This small bubble, which was not patched, starts growing on its own seen in Fig. 13(e). A fully developed vapor bubble can be seen detaching from the heated surface in Fig. 13(f). This shows that the simulation being performed works, which was the motivation to carry out the boiling study. The temperature distribution observed at the divergent end exhibits significant variations due to multiple bubbles growing under the tapered block. This phenomenon contributes to surface cooling and promotes a strong interaction between the cold fluid and the liquid heated at the surface.

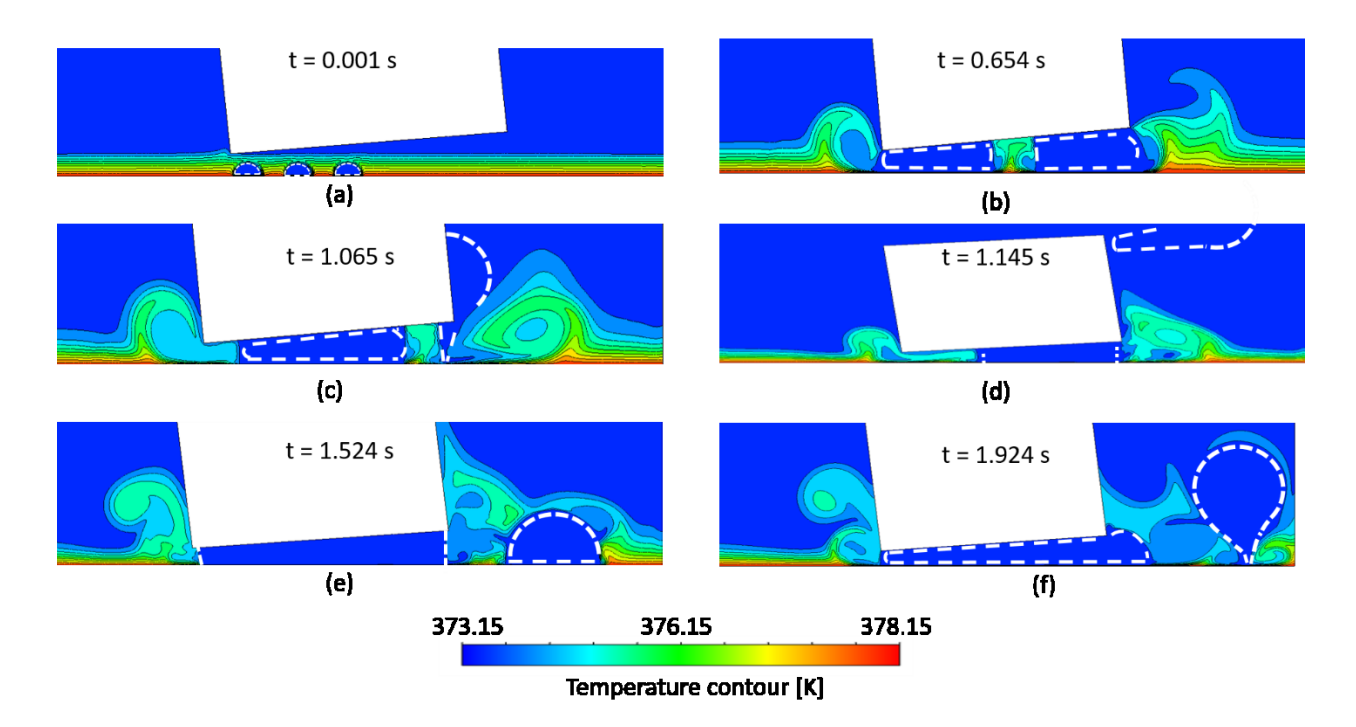


FIGURE 13: Temperature contours of boiling simulation showing growth of three vapor bubble (marked with white dotted boundary) at 1 mm distance from each other, in water at atmospheric conditions, fluid recirculation, and suppression of thermal boundary layer for a taper angle of 5°. No air injection, bubble grows from liquid evaporation at the interface.

Figure 14 shows the computed heat transfer coefficients at multiple instances of time during the bubble growth process through the taper microgap. Fig. 14(a) shows the case of bubble growing from the convergent end. The results in Fig. 14(a) indicate that when the interface recedes (t < 1.89 s), the heat transfer coefficient decays in a small distance from the interface. However, when the interface begins to advance and before departure (1.89 s < t < 2.348), the heat transfer coefficient decays in a larger length from the interface, which is due to the fluid circulations suppressing the thermal boundary layer. After bubble departure (t = 2.43 s), the high local heat transfer coefficient occurs in a larger length from the interface (the influence region is about 1 mm), which is due to the fluid flow rewetting the surface near the trailing edge. Fig. 14(b) shows the case of bubble growing from the divergent end. The results in Fig. 14(b) indicate that when the interface advances (t < 0.243 s), the decrease in the heat transfer coefficient occurs in a small region near the interface. However, when the bubble moves to the inside of the tapered microgap (0.243 s < t < 0.437), the region with an enhanced heat transfer coefficient becomes wider (the influence region is about 0.8 mm), which is due to cold fluid rewetting the surface as the bubble moves. When the bubble continues to recede (growing stage t = 1.89 s), the heat transfer coefficient decays in a small distance from the interface.

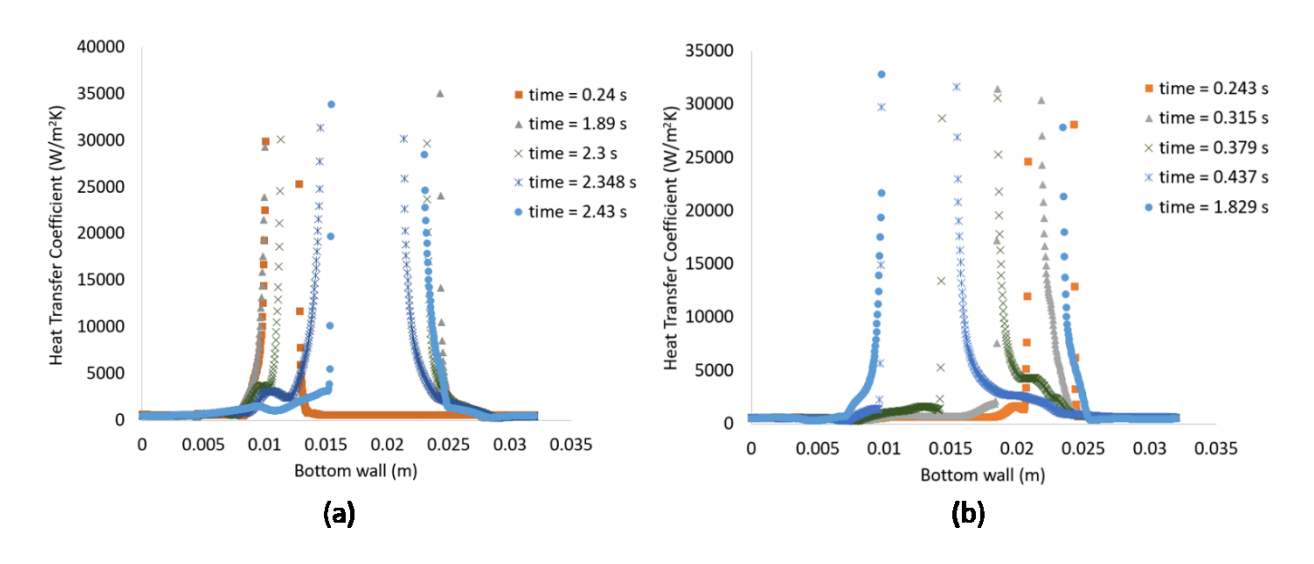


Figure 14: Variation of the local heat transfer coefficient at different times during one bubble cycle for the cases of (a) bubble starting at convergent end, and (b) bubble starting at divergent end.

5. Conclusion

The present study conducts a 2D simulation analysis of bubble growth in tapered microgaps with numerical simulations to identify the effect of the fluid properties and tapered angle in the bubble and fluid dynamics behavior. Ansys-Fluent is customized with user-defined-functions (UDFs) accounting for the interfacial heat and mass transport, including a sharp interface and direct calculation of mass transfer with temperature gradients. The study was conducted using air injection and boiling simulation from the conception to the departure of a bubble. The present work simulated bubble growth in a taper microgap with taper angles of 5°, 10°, and 15° and flowrates of 3, 15, and 30 ml/min. The simulation was extended to varying the surface tension from 0.004 to 0.09 N/m and flowrates of 4, 15, 20, and 25 ml/min to find the transition region for the bubble departure. The transition region is where the direction of the bubble departure can be from both convergent and divergent ends of the taper block. Once the results of the air injection were achieved, the air injection was replaced with a heated bottom wall surface. The simulation was validated against the experiments, and good agreement was observed in terms of bubble growth and bubble shapes. The simulation results gave evidence of the fluid behavior during the bubble growth and departure process. The fluid circulation also aids in the separation of the bubble from the preceding bubble and the departure of the bubble. The 2D simulation is capable of producing experimental results. Overall, the simulation reproduces experimental observations at the analyzed flowrate and gives evidence of the relevant parameters influencing the bubble behavior in the tapered microgap.

The present work demonstrates the use of VOF sharp interface modeling in Ansys-Fluent to simulate bubble growth in tapered microgaps. The simulation approach considers a sharp interface rather than interface smearing and the direct calculation of mass transfer with temperature gradients at the interface rather than employing empirical parameters. The work contributes to the analysis of boiling flows by numerically capturing the hydrodynamics and thermal transport phenomena near the bubble edge. Still, the work needs to be further developed to consider the 3D effects which will allow a more accurate identification of the interface curvature effects on the bubble dynamics. The 3D simulation will reveal the way the bubble evolves along the z-axis, which may influence the time of bubble departure and the fluid

dynamics. The development of the 3D simulation should consider adaptive mesh refinement to ensure achieving accurate sharp interface thermal modeling within reasonable computational times.

The study varied the taper angles at 5°, 10°, and 15° while keeping the flowrate at 3 ml/min. The results showed that squeezing of the bubble between the taper and the bottom wall leads to the bubble escaping towards the divergent end and helps maintain flow stability in the system. The time of departure and the volume of the bubble escaping the taper increases with the increment of the taper angle. For quicker removal of bubble lower taper angles should be used, for higher volume of air bubble removal higher taper angles should be used. To understand the effect of the flowrate, the taper angle was kept constant at 5°, while the flowrate was varied between 3 and 30 ml/min. The results showed that as the flowrate increases beyond 3 ml/min, the departure of the bubble becomes unpredictable until the flowrate reaches 20 ml/min. A transition region exists between 3 ml/min and 20 ml/min where the bubble departs on both ends of the taper geometry. And as the flowrate changes to 20 ml/min and higher, the bubble escapes only at the convergent end.

The effect of the surface tension study showed that similar to a transition region for the flowrate, another transition region exists for the surface tension values. The surface tension was varied between 0.004 N/m to 0.09 N/m. Once the surface tension is below 0.008 N/m, the bubbles only depart at the convergent end. Similarly, the bubbles only depart at the divergent end above the surface tension value of 0.029 N/m. This led to critical surface tension values, where the transition region was between 0.007 and 0.03 N/m, where the bubble departure would be random. The simulation with ethylene glycol and ethanol showed that the time of departure of the bubble decreases at lower surface tension values, which may be due to a reduction in the resistance of the bubble to move along the microgap.

Results with heat transfer indicated that the numerical model is capable of capturing the bubble growth process along with the development of thermal boundary layers near the contact line. It was observed that bubble growth in tapered microgap leads to strong fluid circulations that suppress the thermal boundary layer near the surface. Temperature contours indicated a significant influence of the bubble growth on the liquid temperatures near the heated surface. Computation of the heat transfer coefficient indicated high values in a range of 1 mm from the bubble edge due to fluid flow when the bubble moves along the tapered microgap. Overall, the results in the present work indicate that multiphase flow modeling identifies the thermal and fluid dynamic behavior driving the high heat dissipation observed in tapered microgaps.

Acknowledgment:

The authors acknowledge the financial support provided by the National Science Foundation (NSF) under Grant No. CBET-2,022,614.

References:

- [1] A. Habibi Khalaj and S. K. Halgamuge, "A Review on efficient thermal management of air- and liquid-cooled data centers: From chip to the cooling system," *Applied Energy*, vol. 205, pp. 1165–1188, Nov. 2017, doi: 10.1016/j.apenergy.2017.08.037.
- [2] Y. Sun, G. Chen, S. Zhang, Y. Tang, J. Zeng, and W. Yuan, "Pool boiling performance and bubble dynamics on microgrooved surfaces with reentrant cavities," *Applied Thermal Engineering*, vol. 125, pp. 432–442, Oct. 2017, doi: 10.1016/j.applthermaleng.2017.07.044.

- [3] L. L. Manetti, G. Ribatski, R. R. de Souza, and E. M. Cardoso, "Pool boiling heat transfer of HFE-7100 on metal foams," *Experimental Thermal and Fluid Science*, vol. 113, p. 110025, May 2020, doi: 10.1016/j.expthermflusci.2019.110025.
- [4] L. Duan, B. Liu, B. Qi, Y. Zhang, and J. Wei, "Pool boiling heat transfer on silicon chips with non-uniform micro-pillars," *International Journal of Heat and Mass Transfer*, vol. 151, p. 119456, Apr. 2020, doi: 10.1016/j.ijheatmasstransfer.2020.119456.
- [5] Y. Zhang, D. Lu, Z. Wang, X. Fu, Q. Cao, and Y. Yang, "Experimental investigation on pool-boiling of C-shape heat exchanger bundle used in PRHR HX," *Applied Thermal Engineering*, vol. 114, pp. 186–195, Mar. 2017, doi: 10.1016/j.applthermaleng.2016.11.185.
- [6] M. S. Kamel and F. Lezsovits, "Enhancement of pool boiling heat transfer performance using dilute cerium oxide/water nanofluid: An experimental investigation," *International Communications in Heat and Mass Transfer*, vol. 114, p. 104587, May 2020, doi: 10.1016/j.icheatmasstransfer.2020.104587.
- [7] A. K. Dewangan, A. Kumar, and R. Kumar, "Experimental Study of Nucleate Pool Boiling of R-134a and R-410a on a Porous Surface," *Heat Transfer Engineering*, vol. 40, no. 15, pp. 1249–1258, Sep. 2019, doi: 10.1080/01457632.2018.1460922.
- [8] L. Lin and M. A. Kedzierski, "Review of low-GWP refrigerant pool boiling heat transfer on enhanced surfaces," *International Journal of Heat and Mass Transfer*, vol. 131, pp. 1279–1303, Mar. 2019, doi: 10.1016/j.ijheatmasstransfer.2018.11.142.
- [9] C. Aswin Karthik, P. Kalita, X. Cui, and X. Peng, "Thermal management for prevention of failures of lithium ion battery packs in electric vehicles: A review and critical future aspects," *Energy Storage*, vol. 2, no. 3, p. e137, 2020, doi: 10.1002/est2.137.
- [10] M. Al-Zareer, I. Dincer, and M. A. Rosen, "A novel phase change based cooling system for prismatic lithium ion batteries," *International Journal of Refrigeration*, vol. 86, pp. 203–217, Feb. 2018, doi: 10.1016/j.ijrefrig.2017.12.005.
- [11] C.-J. Kuo and Y. Peles, "Flow Boiling Instabilities in Microchannels and Means for Mitigation by Reentrant Cavities," *Journal of Heat Transfer*, vol. 130, no. 072402, May 2008, doi: 10.1115/1.2908431.
- [12] C. Li, X. Fang, and Q. Dai, "Two-phase flow boiling instabilities: A review," *Annals of Nuclear Energy*, vol. 173, p. 109099, Aug. 2022, doi: 10.1016/j.anucene.2022.109099.
- [13] B. Wang, Y. Hu, Y. He, N. Rodionov, and J. Zhu, "Dynamic instabilities of flow boiling in microchannels: A review," *Applied Thermal Engineering*, vol. 214, p. 118773, Sep. 2022, doi: 10.1016/j.applthermaleng.2022.118773.
- [14] L. Bureš and Y. Sato, "On the modelling of the transition between contact-line and microlayer evaporation regimes in nucleate boiling," *Journal of Fluid Mechanics*, vol. 916, p. A53, Jun. 2021, doi: 10.1017/jfm.2021.204.
- [15] A. Urbano, S. Tanguy, G. Huber, and C. Colin, "Direct numerical simulation of nucleate boiling in micro-layer regime," *International Journal of Heat and Mass Transfer*, vol. 123, pp. 1128–1137, Aug. 2018, doi: 10.1016/j.ijheatmasstransfer.2018.02.104.
- [16] Z. Chen, F. Wu, and Y. Utaka, "Numerical simulation of thermal property effect of heat transfer plate on bubble growth with microlayer evaporation during nucleate pool boiling," *International Journal of Heat and Mass Transfer*, vol. 118, pp. 989–996, Mar. 2018, doi: 10.1016/j.ijheatmasstransfer.2017.11.083.
- [17] Y. Sato and B. Niceno, "Nucleate pool boiling simulations using the interface tracking method: Boiling regime from discrete bubble to vapor mushroom region," *International Journal of Heat and Mass Transfer*, vol. 105, pp. 505–524, Feb. 2017, doi: 10.1016/j.ijheatmasstransfer.2016.10.018.

- [18] G. Son, N. Ramanujapu, and V. K. Dhir, "Numerical Simulation of Bubble Merger Process on a Single Nucleation Site During Pool Nucleate Boiling," *Journal of Heat Transfer*, vol. 124, no. 1, pp. 51–62, Aug. 2001, doi: 10.1115/1.1420713.
- [19] G. Son and V. K. Dhir, "Numerical Simulation of Saturated Film Boiling on a Horizontal Surface," *Journal of Heat Transfer*, vol. 119, no. 3, pp. 525–533, Aug. 1997, doi: 10.1115/1.2824132.
- [20] Y. Wang and J. M. Wu, "Numerical simulation on single bubble behavior during Al2O3/H2O nanofluids flow boiling using Moving Particle Simi-implicit method," *Progress in Nuclear Energy*, vol. 85, pp. 130–139, Nov. 2015, doi: 10.1016/j.pnucene.2015.06.017.
- [21] S. Dou, L. Hao, and H. Liu, "Numerical study of bubble behaviors and heat transfer in pool boiling of water/NaCl solutions using the lattice Boltzmann method," *International Journal of Thermal Sciences*, vol. 170, p. 107158, Dec. 2021, doi: 10.1016/j.ijthermalsci.2021.107158.
- [22] G. Liang and I. Mudawar, "Review of pool boiling enhancement by surface modification," *International Journal of Heat and Mass Transfer*, vol. 128, pp. 892–933, Jan. 2019, doi: 10.1016/j.ijheatmasstransfer.2018.09.026.
- [23] L. Qiu, S. Dubey, F. H. Choo, and F. Duan, "Recent developments of jet impingement nucleate boiling," *International Journal of Heat and Mass Transfer*, vol. 89, pp. 42–58, Oct. 2015, doi: 10.1016/j.ijheatmasstransfer.2015.05.025.
- [24] D. Toghraie, "Numerical thermal analysis of water's boiling heat transfer based on a turbulent jet impingement on heated surface," *Physica E: Low-dimensional Systems and Nanostructures*, vol. 84, pp. 454–465, Oct. 2016, doi: 10.1016/j.physe.2016.07.017.
- [25] S. Ndao, Y. Peles, and M. K. Jensen, "Experimental investigation of flow boiling heat transfer of jet impingement on smooth and micro structured surfaces," *International Journal of Heat and Mass Transfer*, vol. 55, no. 19, pp. 5093–5101, Sep. 2012, doi: 10.1016/j.ijheatmasstransfer.2012.05.009.
- [26] G. Liang and I. Mudawar, "Review of spray cooling Part 1: Single-phase and nucleate boiling regimes, and critical heat flux," *International Journal of Heat and Mass Transfer*, vol. 115, pp. 1174–1205, Dec. 2017, doi: 10.1016/j.ijheatmasstransfer.2017.06.029.
- [27] G. Liang and I. Mudawar, "Review of spray cooling Part 2: High temperature boiling regimes and quenching applications," *International Journal of Heat and Mass Transfer*, vol. 115, pp. 1206–1222, Dec. 2017, doi: 10.1016/j.ijheatmasstransfer.2017.06.022.
- [28] Z. Zhang, P.-X. Jiang, X.-L. Ouyang, J.-N. Chen, and D. M. Christopher, "Experimental investigation of spray cooling on smooth and micro-structured surfaces," *International Journal of Heat and Mass Transfer*, vol. 76, pp. 366–375, Sep. 2014, doi: 10.1016/j.ijheatmasstransfer.2014.04.010.
- [29] C. Guo, X. Hu, W. Cao, D. Yu, and D. Tang, "Effect of mechanical vibration on flow and heat transfer characteristics in rectangular microgrooves," *Applied Thermal Engineering*, vol. 52, no. 2, pp. 385–393, Apr. 2013, doi: 10.1016/j.applthermaleng.2012.12.010.
- [30] A. E. Kabeel, E. M. S. El-Said, and S. A. Dafea, "A review of magnetic field effects on flow and heat transfer in liquids: Present status and future potential for studies and applications," *Renewable and Sustainable Energy Reviews*, vol. 45, pp. 830–837, May 2015, doi: 10.1016/j.rser.2015.02.029.
- [31] B. J. Jones, J. P. McHale, and S. V. Garimella, "The Influence of Surface Roughness on Nucleate Pool Boiling Heat Transfer," *Journal of Heat Transfer*, vol. 131, no. 12, Oct. 2009, doi: 10.1115/1.3220144.
- [32] S. Launay, A. G. Fedorov, Y. Joshi, A. Cao, and P. M. Ajayan, "Hybrid micro-nano structured thermal interfaces for pool boiling heat transfer enhancement," *Microelectronics Journal*, vol. 37, no. 11, pp. 1158–1164, Nov. 2006, doi: 10.1016/j.mejo.2005.07.016.
- [33] D. E. Kim, D. I. Yu, D. W. Jerng, M. H. Kim, and H. S. Ahn, "Review of boiling heat transfer enhancement on micro/nanostructured surfaces," *Experimental Thermal and Fluid Science*, vol. 66, pp. 173–196, Sep. 2015, doi: 10.1016/j.expthermflusci.2015.03.023.

- [34] D. Deng, J. Feng, Q. Huang, Y. Tang, and Y. Lian, "Pool boiling heat transfer of porous structures with reentrant cavities," *International Journal of Heat and Mass Transfer*, vol. 99, pp. 556–568, Aug. 2016, doi: 10.1016/j.ijheatmasstransfer.2016.04.015.
- [35] W. H. Azmi, M. Z. Sharif, T. M. Yusof, R. Mamat, and A. A. M. Redhwan, "Potential of nanorefrigerant and nanolubricant on energy saving in refrigeration system A review," *Renewable and Sustainable Energy Reviews*, vol. 69, pp. 415–428, Mar. 2017, doi: 10.1016/j.rser.2016.11.207.
- [36] A. K. Das, P. K. Das, and P. Saha, "Nucleate boiling of water from plain and structured surfaces," Experimental Thermal and Fluid Science, vol. 31, no. 8, pp. 967–977, Aug. 2007, doi: 10.1016/j.expthermflusci.2006.10.006.
- [37] S. G. Kandlikar, "Fundamental issues related to flow boiling in minichannels and microchannels," *Experimental Thermal and Fluid Science*, vol. 26, no. 2, pp. 389–407, Jun. 2002, doi: 10.1016/S0894-1777(02)00150-4.
- [38] A. Mukherjee and S. G. Kandlikar, "The effect of inlet constriction on bubble growth during flow boiling in microchannels," *International Journal of Heat and Mass Transfer*, vol. 52, no. 21, pp. 5204–5212, Oct. 2009, doi: 10.1016/j.ijheatmasstransfer.2009.04.025.
- [39] S. G. Kandlikar, T. Widger, A. Kalani, and V. Mejia, "Enhanced Flow Boiling Over Open Microchannels With Uniform and Tapered Gap Manifolds," *Journal of Heat Transfer*, vol. 135, no. 061401, May 2013, doi: 10.1115/1.4023574.
- [40] K. Balasubramanian, P. S. Lee, C. J. Teo, and S. K. Chou, "Flow boiling heat transfer and pressure drop in stepped fin microchannels," *International Journal of Heat and Mass Transfer*, vol. 67, pp. 234–252, Dec. 2013, doi: 10.1016/j.ijheatmasstransfer.2013.08.023.
- [41] A. Kalani and S. G. Kandlikar, "Flow patterns and heat transfer mechanisms during flow boiling over open microchannels in tapered manifold (OMM)," *International Journal of Heat and Mass Transfer*, vol. 89, pp. 494–504, Oct. 2015, doi: 10.1016/j.ijheatmasstransfer.2015.05.070.
- [42] D. C. Moreira, G. Ribatski, and S. G. Kandlikar, "Effects of Taper Configurations on Heat Transfer and Pressure Drop in Single-Phase Flows in Microgaps," p. 6, 2020.
- [43] T. S. Emery, E. Del Plato, S. G. Kandlikar, and A. Chauhan, "CPU cooling with a thermosiphon loop with tapered manifold (OMM)," in 2017 16th IEEE Intersociety Conference on Thermal and Thermomechanical Phenomena in Electronic Systems (ITherm), May 2017, pp. 864–870. doi: 10.1109/ITHERM.2017.7992576.
- [44] A. Chauhan and S. G. Kandlikar, "Characterization of a dual taper thermosiphon loop for CPU cooling in data centers," *Applied Thermal Engineering*, vol. 146, pp. 450–458, Jan. 2019, doi: 10.1016/j.applthermaleng.2018.10.010.
- [45] A. Chauhan and S. G. Kandlikar, "High Heat Flux Dissipation Using Symmetric Dual-Taper Manifold in Pool Boiling," presented at the ASME 2019 17th International Conference on Nanochannels, Microchannels, and Minichannels, American Society of Mechanical Engineers Digital Collection, Oct. 2019. doi: 10.1115/ICNMM2019-4292.
- [46] A. Chauhan and S. G. Kandlikar, "Geometrical effects on heat transfer mechanisms during pool boiling in Dual Tapered Microgap with HFE7000," *International Journal of Heat and Mass Transfer*, vol. 183, p. 122165, Feb. 2022, doi: 10.1016/j.ijheatmasstransfer.2021.122165.
- [47] A. Chauhan and S. G. Kandlikar, "High Speed Imaging of Bubble Interface Motion in a Tapered Microgap," presented at the ASME 2020 18th International Conference on Nanochannels, Microchannels, and Minichannels collocated with the ASME 2020 Heat Transfer Summer Conference and the ASME 2020 Fluids Engineering Division Summer Meeting, American Society of Mechanical Engineers Digital Collection, Oct. 2020. doi: 10.1115/ICNMM2020-1020.

- [48] M. Magnini and O. K. Matar, "Numerical study of the impact of the channel shape on microchannel boiling heat transfer," *International Journal of Heat and Mass Transfer*, vol. 150, p. 119322, Apr. 2020, doi: 10.1016/j.ijheatmasstransfer.2020.119322.
- [49] C. Kunkelmann and P. Stephan, "Numerical simulation of the transient heat transfer during nucleate boiling of refrigerant HFE-7100," *International Journal of Refrigeration*, vol. 33, no. 7, pp. 1221–1228, Nov. 2010, doi: 10.1016/j.ijrefrig.2010.07.013.
- [50] S. Gong and P. Cheng, "Lattice Boltzmann simulations for surface wettability effects in saturated pool boiling heat transfer," *International Journal of Heat and Mass Transfer*, vol. 85, pp. 635–646, Jun. 2015, doi: 10.1016/j.ijheatmasstransfer.2015.02.008.
- [51] Q. Li, Q. J. Kang, M. M. Francois, Y. L. He, and K. H. Luo, "Lattice Boltzmann modeling of boiling heat transfer: The boiling curve and the effects of wettability," *International Journal of Heat and Mass Transfer*, vol. 85, pp. 787–796, Jun. 2015, doi: 10.1016/j.ijheatmasstransfer.2015.01.136.
- [52] T. Sun, W. Li, and S. Yang, "Numerical simulation of bubble growth and departure during flow boiling period by lattice Boltzmann method," *International Journal of Heat and Fluid Flow*, vol. 44, pp. 120–129, Dec. 2013, doi: 10.1016/j.ijheatfluidflow.2013.05.003.
- [53] S. Gong and P. Cheng, "Lattice Boltzmann simulation of periodic bubble nucleation, growth and departure from a heated surface in pool boiling," *International Journal of Heat and Mass Transfer*, vol. 64, pp. 122–132, Sep. 2013, doi: 10.1016/j.ijheatmasstransfer.2013.03.058.
- [54] B. Mohammedi, S. Hanini, A. Ararem, and M. Nacim, "Simulation of nucleate boiling under ANSYS-FLUENT code by using RPI model coupling with artificial neural networks," *Nuclear Science and Techniques*, vol. 26, p. 040601, Aug. 2015, doi: 10.13538/j.1001-8042/nst.26.040601.
- [55] M. Magnini, B. Pulvirenti, and J. R. Thome, "Numerical investigation of hydrodynamics and heat transfer of elongated bubbles during flow boiling in a microchannel," *International Journal of Heat and Mass Transfer*, vol. 59, pp. 451–471, Apr. 2013, doi: 10.1016/j.ijheatmasstransfer.2012.12.010.
- [56] R. Zhuan and W. Wang, "Flow pattern of boiling in micro-channel by numerical simulation," *International Journal of Heat and Mass Transfer*, vol. 55, no. 5, pp. 1741–1753, Feb. 2012, doi: 10.1016/j.ijheatmasstransfer.2011.11.029.
- [57] A. Mukherjee and S. G. Kandlikar, "Numerical simulation of growth of a vapor bubble during flow boiling of water in a microchannel," *Microfluid Nanofluid*, vol. 1, no. 2, pp. 137–145, May 2005, doi: 10.1007/s10404-004-0021-8.
- [58] R. Zhuan and W. Wang, "Simulation on nucleate boiling in micro-channel," *International Journal of Heat and Mass Transfer*, vol. 53, no. 1, pp. 502–512, Jan. 2010, doi: 10.1016/j.ijheatmasstransfer.2009.08.019.
- [59] R. Jafari and T. Okutucu-Özyurt, "Numerical simulation of flow boiling from an artificial cavity in a microchannel," *International Journal of Heat and Mass Transfer*, vol. 97, pp. 270–278, Jun. 2016, doi: 10.1016/j.ijheatmasstransfer.2016.02.028.
- [60] A. Ferrari, M. Magnini, and J. R. Thome, "Numerical analysis of slug flow boiling in square microchannels," *International Journal of Heat and Mass Transfer*, vol. 123, pp. 928–944, Aug. 2018, doi: 10.1016/j.ijheatmasstransfer.2018.03.012.
- [61] J. Broughton and Y. K. Joshi, "Flow boiling in geometrically modified microchannels," *Physics of Fluids*, vol. 33, no. 10, p. 103308, Oct. 2021, doi: 10.1063/5.0062585.
- [62] Y. Guo, C.-Y. Zhu, L. Gong, and Z.-B. Zhang, "Numerical simulation of flow boiling heat transfer in microchannel with surface roughness," *International Journal of Heat and Mass Transfer*, vol. 204, p. 123830, May 2023, doi: 10.1016/j.ijheatmasstransfer.2022.123830.
- [63] K. Vontas, M. Andredaki, A. Georgoulas, N. Miché, and M. Marengo, "The effect of surface wettability on flow boiling characteristics within microchannels," *International Journal of Heat and Mass Transfer*, vol. 172, p. 121133, Jun. 2021, doi: 10.1016/j.ijheatmasstransfer.2021.121133.

- [64] U. K. Alugoju, S. K. Dubey, and A. Javed, "3D Transient heat transfer analysis and flow visualization study in diverging microchannel for instability mitigated two-phase flow: A numerical study," *International Journal of Heat and Mass Transfer*, vol. 160, p. 120212, Oct. 2020, doi: 10.1016/j.ijheatmasstransfer.2020.120212.
- [65] "Numerical investigation of hydrodynamics and heat transfer of elongated bubbles during flow boiling in a microchannel," *International Journal of Heat and Mass Transfer*, vol. 59, pp. 451–471, Apr. 2013, doi: 10.1016/j.ijheatmasstransfer.2012.12.010.
- [66] S. P. Shipkowski and I. Perez-Raya, "Precise and analytical calculation of interface surface area in sharp interfaces and multiphase modeling," *International Journal of Heat and Mass Transfer*, vol. 202, p. 123683, Mar. 2023, doi: 10.1016/j.ijheatmasstransfer.2022.123683.
- [67] S. Zhao, J. Zhang, and M.-J. Ni, "Boiling and evaporation model for liquid-gas flows: A sharp and conservative method based on the geometrical VOF approach," *Journal of Computational Physics*, vol. 452, p. 110908, Mar. 2022, doi: 10.1016/j.jcp.2021.110908.
- [68] I. Yeo and S. Lee, "2D computational investigation into transport phenomena of subcooled and saturated flow boiling in large length to diameter ratio micro-channel heat sinks," *International Journal of Heat and Mass Transfer*, vol. 183, p. 122128, Feb. 2022, doi: 10.1016/j.ijheatmasstransfer.2021.122128.
- [69] D. Sun, J. Xu, and Q. Chen, "Modeling of the Evaporation and Condensation Phase-Change Problems with FLUENT," *Numerical Heat Transfer, Part B: Fundamentals*, vol. 66, no. 4, pp. 326–342, Oct. 2014, doi: 10.1080/10407790.2014.915681.
- [70] S. Rajendran, R. M. Manglik, and M. A. Jog, "New Property Averaging Scheme for Volume of Fluid Method for Two-Phase Flows With Large Viscosity Ratios," *Journal of Fluids Engineering*, vol. 144, no. 6, Feb. 2022, doi: 10.1115/1.4053548.
- [71] F. Garoosi and K. Hooman, "Numerical simulation of multiphase flows using an enhanced Volume-of-Fluid (VOF) method," *International Journal of Mechanical Sciences*, vol. 215, p. 106956, Feb. 2022, doi: 10.1016/j.ijmecsci.2021.106956.
- [72] S. Fostiropoulos, G. Strotos, N. Nikolopoulos, and M. Gavaises, "Numerical investigation of heavy fuel oil droplet breakup enhancement with water emulsions," *Fuel*, vol. 278, p. 118381, Oct. 2020, doi: 10.1016/j.fuel.2020.118381.
- [73] C.-W. Lin, Y.-C. Lin, R. Kumar, M.-C. Lin, and H.-Y. Hsu, "A numerical study of microtube geometry effect on flow boiling using the volume of fluid method," *International Journal of Heat and Mass Transfer*, vol. 199, p. 123477, Dec. 2022, doi: 10.1016/j.ijheatmasstransfer.2022.123477.
- [74] C. R. Kharangate and I. Mudawar, "Review of computational studies on boiling and condensation," *International Journal of Heat and Mass Transfer*, vol. 108, pp. 1164–1196, May 2017, doi: 10.1016/j.ijheatmasstransfer.2016.12.065.
- [75] L. Bureš and Y. Sato, "Direct numerical simulation of evaporation and condensation with the geometric VOF method and a sharp-interface phase-change model," *International Journal of Heat and Mass Transfer*, vol. 173, p. 121233, Jul. 2021, doi: 10.1016/j.ijheatmasstransfer.2021.121233.
- [76] T. Ménard, S. Tanguy, and A. Berlemont, "Coupling level set/VOF/ghost fluid methods: Validation and application to 3D simulation of the primary break-up of a liquid jet," *International Journal of Multiphase Flow*, vol. 33, no. 5, pp. 510–524, May 2007, doi: 10.1016/j.ijmultiphaseflow.2006.11.001.
- [77] M. Naghashnejad, H. Shabgard, and T. L. Bergman, "Computational Simulation of Spontaneous Liquid Penetration and Depression Between Vertical Parallel Plates," *Journal of Fluids Engineering*, vol. 143, no. 5, Feb. 2021, doi: 10.1115/1.4049683.
- [78] X. Shang, X. Zhang, T.-B. Nguyen, and T. Tran, "Direct numerical simulation of evaporating droplets based on a sharp-interface algebraic VOF approach," *International Journal of Heat and Mass Transfer*, vol. 184, p. 122282, Mar. 2022, doi: 10.1016/j.ijheatmasstransfer.2021.122282.

- [79] "A sharp-interface phase change model for a mass-conservative interface tracking method," *Journal of Computational Physics*, vol. 249, pp. 127–161, Sep. 2013, doi: 10.1016/j.jcp.2013.04.035.
- [80] Y. Sato and B. Niceno, "Pool boiling simulation using an interface tracking method: From nucleate boiling to film boiling regime through critical heat flux," *International Journal of Heat and Mass Transfer*, vol. 125, pp. 876–890, Oct. 2018, doi: 10.1016/j.ijheatmasstransfer.2018.04.131.
- [81] "A depletable micro-layer model for nucleate pool boiling," *Journal of Computational Physics*, vol. 300, pp. 20–52, Nov. 2015, doi: 10.1016/j.jcp.2015.07.046.
- [82] "Evaporation model for interfacial flows based on a continuum-field representation of the source terms," *Journal of Computational Physics*, vol. 227, no. 11, pp. 5871–5895, May 2008, doi: 10.1016/j.jcp.2008.02.020.
- [83] C. Kunkelmann and P. Stephan, "CFD Simulation of Boiling Flows Using the Volume-of-Fluid Method within OpenFOAM," *Numerical Heat Transfer, Part A: Applications*, vol. 56, no. 8, pp. 631–646, Nov. 2009, doi: 10.1080/10407780903423908.
- [84] "A numerical investigation of nucleate boiling at a constant surface temperature," *Applied Thermal Engineering*, vol. 88, pp. 248–257, Sep. 2015, doi: 10.1016/j.applthermaleng.2014.09.022.
- [85] M. Yazdani, T. Radcliff, M. Soteriou, and A. A. Alahyari, "A high-fidelity approach towards simulation of pool boiling," *Physics of Fluids*, vol. 28, no. 1, p. 012111, Jan. 2016, doi: 10.1063/1.4940042.
- [86] Q. Liu and B. Palm, "Numerical study of bubbles rising and merging during convective boiling in micro-channels," *Applied Thermal Engineering*, vol. 99, pp. 1141–1151, Apr. 2016, doi: 10.1016/j.applthermaleng.2016.01.116.
- [87] M. Akhtar and S. Kleis, "A volume of fluid phase change model on adaptive octree grids," in *Film and Nucleate Boiling Processes*, ASTM International, 2012.
- [88] "Boiling flow simulations on adaptive octree grids," *International Journal of Multiphase Flow*, vol. 53, pp. 88–99, Jul. 2013, doi: 10.1016/j.ijmultiphaseflow.2013.01.008.
- [89] S. W. J. Welch and J. Wilson, "A Volume of Fluid Based Method for Fluid Flows with Phase Change," Journal of Computational Physics, vol. 160, no. 2, pp. 662–682, May 2000, doi: 10.1006/jcph.2000.6481.
- [90] G. Son and V. K. Dhir, "Numerical simulation of nucleate boiling on a horizontal surface at high heat fluxes," *International Journal of Heat and Mass Transfer*, vol. 51, no. 9, pp. 2566–2582, May 2008, doi: 10.1016/j.ijheatmasstransfer.2007.07.046.
- [91] J. Wu and V. K. Dhir, "Numerical Simulation of Dynamics and Heat Transfer Associated With a Single Bubble in Subcooled Boiling and in the Presence of Noncondensables," *Journal of Heat Transfer*, vol. 133, no. 041502, Jan. 2011, doi: 10.1115/1.4000979.
- [92] E. Aktinol and V. K. Dhir, "NUMERICAL SIMULATION OF THE EFFECT OF CONTACT ANGLE ON THE THERMAL RESPONSE OF THE SOLID DURING NUCLEATE POOL BOILING," *IPHT*, vol. 2, no. 4, 2014, doi: 10.1615/InterfacPhenomHeatTransfer.2015012160.
- [93] R. Bardia and M. F. Trujillo, "Assessing the physical validity of highly-resolved simulation benchmark tests for flows undergoing phase change," *International Journal of Multiphase Flow*, vol. 112, pp. 52–62, Mar. 2019, doi: 10.1016/j.ijmultiphaseflow.2018.11.018.
- [94] H. Onishi, T. Goto, M. Haruki, and Y. Tada, "Volume of fluid-based numerical analysis of a pump-driven phase change heat transport device," *International Journal of Heat and Mass Transfer*, vol. 186, p. 122429, May 2022, doi: 10.1016/j.ijheatmasstransfer.2021.122429.
- [95] E. ÇİFTÇİ, "SIMULATION OF NUCLEATE POOL BOILING HEAT TRANSFER CHARACTERISTICS OF THE AQUEOUS KAOLIN AND BAUXITE NANOFLUIDS," *HTR*, vol. 52, no. 1, 2021, doi: 10.1615/HeatTransRes.2020035191.

- [96] J. Lee, L. E. O'Neill, S. Lee, and I. Mudawar, "Experimental and computational investigation on two-phase flow and heat transfer of highly subcooled flow boiling in vertical upflow," *International Journal of Heat and Mass Transfer*, vol. 136, pp. 1199–1216, Jun. 2019, doi: 10.1016/j.ijheatmasstransfer.2019.03.046.
- [97] R. Kumar and A. K. Das, "Numerical study of boiling of liquid nitrogen at solid and liquid contact planes," *International Journal of Heat and Mass Transfer*, vol. 183, p. 122075, Feb. 2022, doi: 10.1016/j.ijheatmasstransfer.2021.122075.
- [98] M. S. Kamel, M. S. Al-agha, F. Lezsovits, and O. Mahian, "Simulation of pool boiling of nanofluids by using Eulerian multiphase model," *J Therm Anal Calorim*, vol. 142, no. 1, pp. 493–505, Oct. 2020, doi: 10.1007/s10973-019-09180-x.
- [99] P. E. Rodríguez-Ocampo *et al.*, "A 2D Image-Based Approach for CFD Validation of Liquid Mixing in a Free-Surface Condition," *Journal of Applied Fluid Mechanics*, vol. 13, no. 5, pp. 1487–1500, May 2020, doi: 10.36884/jafm.13.05.30909.
- [100] S. Iyer, A. Kumar, J. Coventry, and W. Lipiński, "Heat transfer modelling of an isolated bubble in sodium pool boiling," *International Journal of Thermal Sciences*, vol. 179, p. 107678, Sep. 2022, doi: 10.1016/j.ijthermalsci.2022.107678.
- [101] F. Gibou, L. Chen, D. Nguyen, and S. Banerjee, "A level set based sharp interface method for the multiphase incompressible Navier–Stokes equations with phase change," *Journal of Computational Physics*, vol. 222, no. 2, pp. 536–555, 2007.
- [102] S. V. Patankar, "Chapter Seven-Finishing Touches," *Numerical Heat Transfer and Fluid Flow, New York*, 1980.
- [103] I. Perez-Raya and S. G. Kandlikar, "Discretization and implementation of a sharp interface model for interfacial heat and mass transfer during bubble growth," *International Journal of Heat and Mass Transfer*, vol. 116, pp. 30–49, Jan. 2018, doi: 10.1016/j.ijheatmasstransfer.2017.08.106.
- [104] I. Perez-Raya and S. G. Kandlikar, "Evaporation on a Planar Interface—Numerical Simulation and Theoretical Analysis of Heat and Mass Transport Processes," in *Advances in Heat Transfer*, vol. 48, Elsevier, 2016, pp. 125–190.
- [105] I. Perez-Raya and S. G. Kandlikar, "Numerical modeling of interfacial heat and mass transport phenomena during a phase change using ANSYS-Fluent," *Numerical Heat Transfer, Part B:* Fundamentals, vol. 70, no. 4, pp. 322–339, Oct. 2016, doi: 10.1080/10407790.2016.1215708.
- [106] I. Perez-Raya and S. G. Kandlikar, "Numerical models to simulate heat and mass transfer at sharp interfaces in nucleate boiling," *Numerical Heat Transfer, Part A: Applications*, vol. 74, no. 10, pp. 1583–1610, Nov. 2018, doi: 10.1080/10407782.2018.1543918.
- [107] A. Chauhan and S. G. Kandlikar, "Transforming pool boiling into self-sustained flow boiling through bubble squeezing mechanism in tapered microgaps," *Appl. Phys. Lett.*, vol. 116, no. 8, p. 081601, Feb. 2020, doi: 10.1063/1.5141357.
- [108] P. A. Raghupathi and S. G. Kandlikar, "Bubble growth and departure trajectory under asymmetric temperature conditions," *International Journal of Heat and Mass Transfer*, vol. 95, pp. 824–832, Apr. 2016, doi: 10.1016/j.ijheatmasstransfer.2015.12.058.
- [109] S. G. Kandlikar, "Evaporation Momentum Force and Its Relevance to Boiling Heat Transfer," *Journal of Heat Transfer*, vol. 142, no. 100801, Jul. 2020, doi: 10.1115/1.4047268.